

# ***SNF Modeling and Testing - LANL (FY21)***

## **Fuel Cycle Technology**

***Prepared for  
U.S. Department of Energy  
Spent Fuel & Waste Science and Tech***

***Migdissov, A.***

***Kalintsev, A.***

***Nisbet, H.***

***Alcorn, C.***

***Caporuscio, F.***

***Los Alamos National Laboratory***

***July 21, 2021***

***SF-21LA01030904***

***LA-UR-21-27705***






10/7/2019

**APPENDIX E**  
**NFCSC DOCUMENT COVER SHEET <sup>1</sup>**

Name/Title of Deliverable/Milestone/Revision No. SNF Modeling and Testing-LANL - 1 BCP-SF-2021-02

Work Package Title and Number SNF Modeling and Testing - LANL (FY21)

Work Package WBS Number SF-21LA01030904

Responsible Work Package Manager Artaches Migdissov  
 (Name/Signature) 

Date Submitted

Quality Rigor Level for Deliverable/Milestone <sup>2</sup>	<input type="checkbox"/> QRL-1	<input type="checkbox"/> QRL-2	<input type="checkbox"/> QRL-3	<input type="checkbox"/> QRL-4
	<input type="checkbox"/> Nuclear Data			Lab QA Program <sup>3</sup>

This deliverable was prepared in accordance with Los Alamos National Laboratory  
 (Participant/National Laboratory Name)

QA program which meets the requirements of  
 DOE Order 414.1       NQA-1       Other

**This Deliverable was subjected to:**

Technical Review

Peer Review

**Technical Review (TR)**

**Peer Review (PR)**

**Review Documentation Provided**

**Review Documentation Provided**

- Signed TR Report or,
- Signed TR Concurrence Sheet or,
- Signature of TR Reviewer(s) below

- Signed PR Report or,
- Signed PR Concurrence Sheet or,
- Signature of PR Reviewer(s) below

**Name and Signature of Reviewers**

Kirsten Sauer

\_\_\_\_\_  
 \_\_\_\_\_  
 \_\_\_\_\_

\_\_\_\_\_  
**Kirsten Sauer** Digitally signed by Kirsten Sauer  
 Date: 2021.07.28 10:46:55 -06'00'

**NOTE 1:** Appendix E should be filled out and submitted with the deliverable. Or, if the PICS:NE system permits, completely enter all applicable information in the PICS:NE Deliverable Form. The requirement is to ensure that all applicable information is entered either in the PICS:NE system or by using the NTRD Document Cover Sheet.

- In some cases there may be a milestone where an item is being fabricated, maintenance is being performed on a facility, or a document is being issued through a formal document control process where it specifically calls out a formal review of the document. In these cases, documentation (e.g., inspection report, maintenance request, work planning package documentation or the documented review of the issued document through the document control process) of the completion of the activity, along with the Document Cover Sheet, is sufficient to demonstrate achieving the milestone.

**NOTE 2:** If QRL 1, 2, or 3 is not assigned, then the QRL 4 box must be checked, and the work is understood to be performed using laboratory QA requirements. This includes any deliverable developed in conformance with the respective National Laboratory / Participant, DOE or NNSA-approved QA Program.

**NOTE 3:** If the lab has an NQA-1 program and the work to be conducted requires an NQA-1 program, then the QRL-1 box must be checked in the work Package and on the Appendix E cover sheet and the work must be performed in accordance with the Lab's NQA-1 program. The QRL-4 box should not be checked.

**DISCLAIMER**

This information was prepared as an account of work sponsored by an agency of the U.S. Government. Neither the U.S. Government nor any agency thereof, nor any of their employees, makes any warranty, expressed or implied, or assumes any legal liability or responsibility for the accuracy, completeness, or usefulness, of any information, apparatus, product, or process disclosed, or represents that its use would not infringe privately owned rights. References herein to any specific commercial product, process, or service by trade name, trade mark, manufacturer, or otherwise, does not necessarily constitute or imply its endorsement, recommendation, or favoring by the U.S. Government or any agency thereof. The views and opinions of authors expressed herein do not necessarily state or reflect those of the U.S. Government or any agency thereof.

**STANDARD CONTRACT DISCLAIMER**

This is a technical report that does not take into account the contractual limitations under the Standard Contract for Disposal of Spent Nuclear Fuel and/or High-Level Radioactive Waste (Standard Contract) (10 CFR Part 961). For example, under the provisions of the Standard Contract, DOE does not consider spent nuclear fuel in multi-assembly canisters to be an acceptable waste form, absent a mutually agreed to contract amendment. To the extent discussions or recommendations in this report conflict with the provisions of the Standard Contract, the Standard Contract provisions prevail.

## SUMMARY

This contribution consists of two parts, the first of which reports findings from FY21 on the behavior of uranium in carbonate bearing aqueous solutions at elevated temperatures up to 250 °C. This study demonstrates that the aqueous transport of U by carbonate aqueous complexes is significant only at temperatures below 120-140 °C. At higher temperatures, carbonate complexes of U destabilize and, thus, will not predominate in aqueous solutions with carbonate concentrations typically associated with natural surface waters and deep geological fluids. Considering that many models assume carbonate as a main vehicle for U transport in natural fluids, this finding has important consequences, and likely necessitates a re-evaluation of current models that assess the transport of U. The results of this study have been reported in a paper published by *Communications Chemistry (Nature Research)* (Kalintsev et al., *in press*).

The second part of this report is devoted to re-visiting experimental data on the aqueous speciation of U, reported at previous stages of the project. Since 2018, the behavior of U in hydrothermal solutions has been investigated for a set of aqueous systems, including chloride- and sulfate-bearing fluids. This data has been reported in a set of contributions published in *Geochimica et Cosmochimica Acta* and *J. Phys. Chem. B* (Migdisov et al., 2018a; Alcorn et al., 2019; Kalintsev et al., 2019). Incorporation of this data into predictive thermodynamic models requires the representation of experimental data in the form of Equations of State (EoS) suitable for modeling with major thermodynamic codes. Thus, the second part of this contribution documents the efforts aimed at fitting the published experimental data, together with previously reported data available in the literature, to the Modified Ryzhenko-Bryzgalin (MRB) and the Helgeson-Kirkham-Flowers (HKF) models and reports the tables of species-specific parameters for these equations of state.



## CONTENTS

SUMMARY .....	v
ACRONYMS .....	xi
1. URANIUM SPECIATION IN CARBONATE-BEARING HYDROTHERMAL SOLUTIONS .....	12
1.1 BACKGROUND AND OBJECTIVE.....	13
1.2 METHODS.....	14
1.2.1 Raman Spectroscopy .....	14
1.2.2 XAS Experiments.....	15
1.2.3 Solubility Experiments.....	16
1.2.4 Thermodynamic Calculations .....	20
1.3 RESULTS.....	21
1.3.1 Raman Spectroscopy .....	21
1.3.2 X-Ray Absorption Spectroscopy.....	23
1.3.3 Solubility Experiments.....	25
1.4 DISCUSSION .....	33
1.5 CONCLUSION .....	33
2. THERMODYNAMIC PROPERTIES OF URANYL-CHLORIDE AND URANYL-SULFATE AQUEOUS COMPLEXES AT ELEVATED TEMPERATURES .....	34
2.1 INTRODUCTION.....	35
2.2 DATA REPRESENTATION, EOS FORMULATIONS AND DATA FITTING.....	35
2.3 ACKNOWLEDGEMENTS .....	39
2.4 APPENDIX 1. $\text{UO}_2^{2+}/\text{Cl}^-$ CHEMICAL SYSTEM.....	40
2.5 APPENDIX 2. $\text{UO}_2^{2+}/\text{SO}_4^{2-}$ CHEMICAL SYSTEM .....	47
3. REFERENCES .....	55

## FIGURES

Figure 1.1. Schematic diagram of the autoclave system used for solubility experiments. ....	17
Figure 1.2. Major steps in the autoclave solubility technique.....	19
Figure 1.3. Results from the kinetic series conducted at 200°C. Note that equilibrium was essentially reached within 1 day. ....	19
Figure 1.4. Raman spectra of 0.012 m $\text{UO}_2^{2+}$ + 0.1 m $\text{NaHCO}_3$ taken at 25, 50 and 98°C, before and after heating.....	22
Figure 1.5. Raman Spectra of a solution of 0.012 m $\text{UO}_2^{2+}$ and 0.1 m $\text{NaHCO}_3$ collected at 146 °C before and after heating for 67 hours.....	23
Figure 1.6. (a) U LIII-edge k <sup>2</sup> -weighted EXAFS spectra ( $k = 3.0 - 10.5 \text{ \AA}^{-1}$ ) from 25 °C to 125 °C. (b) Corresponding Fourier transform of EXAFS spectra. ....	24
Figure 1.7. Measured and calculated solubilities of $\text{UO}_2(\text{OH})_2$ as functions of calculated carbonate activity.....	29
Figure 1.8. Measured and calculated solubilities of $\text{UO}_2(\text{OH})_2$ plotted as functions of pH at temperature. ....	30
Figure 2.1. The quality of the MRB interpolation performed for the $\text{UO}_2\text{Cl}^+$ formation constants (pK).....	41
Figure 2.2. The quality of the MRB interpolation performed for the $\text{UO}_2\text{Cl}_2$ formation constants (pK).....	42
Figure 2.3. The quality of the MRB interpolation performed for the $\text{UO}_2\text{SO}_4$ formation constants (pK).....	48
Figure 2.4. The quality of the MRB interpolation performed for the $\text{UO}_2(\text{SO}_4)_2^{2-}$ formation constants (pK).....	50



## TABLES

Table 1.1. Compositions and results from all autoclave solubility solutions.....	27
Table 1.2. Formation constants for Equation 1.4. ....	32
Table 1.3. MRB fitting parameters for the $\text{UO}_2\text{OH}^+$ dissociation reaction using values reported in Table 2. ....	32
Table 1.4. Formation constants of Equation 1.4 at a range of temperatures calculated using MRB parameters reported in Table 3. ....	32
Table 2.1. Formation constants (pK) experimentally derived for $\text{UO}_2\text{Cl}^+$ ( $\text{UO}_2^{2+} + \text{Cl}^- = \text{UO}_2\text{Cl}^+$ ) together with the derived parameters for the Modified Ryzhenko-Bryzgalin interpolative EoS, the optimized/interpolated values of formation pK, and errors characterizing quality of the fit.....	40
Table 2.2. Formation constants (pK) experimentally derived for $\text{UO}_2\text{Cl}_2$ ( $\text{UO}_2^{2+} + 2\text{Cl}^- = \text{UO}_2\text{Cl}_2$ ) together with the derived parameters for the Modified Ryzhenko-Bryzgalin interpolative EoS, the interpolated values of formation pK, and errors characterizing quality of the fit. ....	41
Table 2.3. Summarized MRB parameters derived for $\text{UO}_2\text{Cl}^+$ and $\text{UO}_2\text{Cl}_2$ . ....	42
Table 2.4. Initial estimates of HKF parameters for $\text{UO}_2^{2+}/\text{Cl}^-$ species derived using PRONSPREP97 (cal). ....	42
Table 2.5. The HKF optimization performed for $\text{UO}_2\text{Cl}^+$ based on the tabulated apparent Gibbs free energies, derived using the interpolation detailed in Table 2.1. ....	43
Table 2.6. The HKF optimization performed for $\text{UO}_2\text{Cl}_2$ based on the tabulated apparent Gibbs free energies, derived using the interpolation detailed in Table 2.2. ....	44
Table 2.7. Final recommended values for the HKF EoS for $\text{UO}_2\text{Cl}^+$ and $\text{UO}_2\text{Cl}_2$ (cal). ....	45
Table 2.8. Tabulated formation constants (pK = $-\log K$ ) for the reaction $\text{UO}_2^{2+} + \text{Cl}^- = \text{UO}_2\text{Cl}^+$ . ....	45
Table 2.9. Tabulated formation constants (pK = $-\log K$ ) for the reaction $\text{UO}_2^{2+} + 2\text{Cl}^- = \text{UO}_2\text{Cl}_2$ .....	46

---

Table 2.10. Formation constants (pK) experimentally derived for $\text{UO}_2\text{SO}_4$ ( $\text{UO}_2^{2+} + \text{SO}_4^{2-} = \text{UO}_2\text{SO}_4$ ) together with the derived parameters for the Modified Ryzhenko-Bryzgalin interpolative EoS, the optimized/interpolated values of formation pK, and errors characterizing quality of the fit. ....	47
Table 2.11. Formation constants (pK) experimentally derived for $\text{UO}_2(\text{SO}_4)_2^{2-}$ ( $\text{UO}_2^{2+} + 2 \text{SO}_4^{2-} = \text{UO}_2(\text{SO}_4)_2^{2-}$ ) together with the derived parameters for the Modified Ryzhenko-Bryzgalin interpolative EoS, the optimized/interpolated values of formation pK, and errors characterizing quality of the fit. ....	49
Table 2.12. Summarized MRB parameters derived for $\text{UO}_2\text{SO}_4$ and $\text{UO}_2(\text{SO}_4)_2^{2-}$ . ....	50
Table 2.13. Initial estimates of HKF parameters for $\text{UO}_2^{2+}/\text{SO}_4^{2-}$ species derived using PRONSPREP97 (cal). ....	50
Table 2.14. The HKF optimization performed for $\text{UO}_2(\text{SO}_4)$ based on the tabulated apparent Gibbs free energies, derived using the interpolation detailed in Table 2.2. ....	51
Table 2.0.15. The HKF optimization performed for $\text{UO}_2(\text{SO}_4)_2$ based on the tabulated apparent Gibbs free energies, derived using the interpolation detailed in Table 2.2. ....	52
Table 2.0.16. Final recommended values for the HKF EoS for $\text{UO}_2\text{SO}_4$ and $\text{UO}_2(\text{SO}_4)_2^{2-}$ (cal). ....	53
Table 2.0.17. Tabulated formation constants (pK = -log K) for the reaction $\text{UO}_2^{++} + \text{SO}_4^{2-} = \text{UO}_2\text{SO}_4$ . ....	53
Table 2.18. Tabulated formation constants (pK = -log K) for the reaction $\text{UO}_2^{++} + 2\text{SO}_4^{2-} = \text{UO}_2(\text{SO}_4)_2^{2-}$ . ....	54

## **ACRONYMS**

EXAFS – Extended X-Ray Absorption Fine Structure

HDAC – Hydrothermal Diamond Anvil Cell

ICP-MS – Inductively Coupled Plasma Mass Spectrometry

P-XRD – Powder X-Ray Diffraction

SWP – Saturated Water-vapor Pressure

XAS – X-Ray Absorption Spectroscopy

XRD – X-Ray Diffraction

SFWD – Spent Fuel and Waste Disposition

SF – Spent Fuel

EoS – Equation of State

MRB – Modified Ryzhenko-Bryzgalin

HKF – Helgeson-Kirkham-Flowers

- 1. URANIUM SPECIATION IN CARBONATE-BEARING HYDROTHERMAL SOLUTIONS**

## 1.1 BACKGROUND AND OBJECTIVE

A nuclear power plant usually generates over 20 tons of nuclear waste annually with most of it contained in above-the-ground storage (e.g. in pools), providing only a temporary solution to the waste problem (Bruno and Ewing, 2006). Long-term underground disposal, however, must be highly resistant to the eventuality of natural disasters and human intervention, precluding the release of radioactive contaminants to the environment. Thus, the resistance of  $\text{UO}_2$  spent fuels to aqueous corrosion is an essential requirement to prevent the release of U and fission products to the environment (Xu et al., 2000; Guo et al., 2019). If a containment breach and subsequent infiltration of surrounding groundwater into the system occur in the first 50 to 200 years of its lifetime (Hardin et al., 2013), there is a significant possibility that nuclear waste will interact with the water around peak temperature conditions resulting from radionuclide decay. In the case of large DPCs, temperatures can reach  $\sim 300$  °C or higher (Greenburg and Wen, 2013). Thus, in such a scenario, it is critical to understand the solubility of U at elevated temperatures. In general, uranium is most effectively transported by hydrothermal fluids when present in its hexavalent (U(VI)) oxidation state, which, as the uranyl ion ( $\text{UO}_2^{2+}$ ), is highly soluble and forms stable complexes with a range of inorganic ligands, most commonly  $\text{Cl}^-$ ,  $\text{SO}_4^{2-}$ ,  $\text{OH}^-$  and  $\text{CO}_3^{2-}$  (Guillaumont et al., 2003; Bastrakov et al., 2010). Thus, the presence of such ligands serves as a principal way to enhance the uranium carrying capacity of hydrothermal fluids. While naturally dependent upon ligand concentration, the predominance of a given complex is also strongly controlled by fluid pH. Under acidic conditions, uranyl complexes most readily with  $\text{Cl}^-$  and  $\text{SO}_4^{2-}$  (Skirrow, 2009; Bastrakov et al., 2010; Migdisov et al., 2018b; Kalintsev et al., 2019), but sea water, many groundwater systems and a number (though not all) of deep geologic fluids are characterized by near-neutral/slightly alkaline pH ranges (Hem, 1985; Ondruš et al., 2003; Skirrow, 2009; Bastrakov et al., 2010; Staude et al., 2012).

At near-neutral/slightly alkaline pH and under ambient conditions, uranium mobility may be controlled by hydroxyl, biphosphate ( $\text{HPO}_4^{2-}$ ) and carbonate ( $\text{CO}_3^{2-}$ ) complexes (Guillaumont et al., 2003; Skirrow, 2009; Bastrakov et al., 2010). It has been suggested that under such pH conditions and at elevated temperatures uranyl-carbonate complexes in particular could play an

important role in uranium transport (Cuney, 1978; McLennan and Taylor, 1979; Higgins, 1980; Bailey and Vala Ragnarsdottir, 1994; Ondruš et al., 2003; Skirrow, 2009; Bastrakov et al., 2010; Staude et al., 2012; Ewing, 2015; Zhang et al., 2017). However, to date, uranyl carbonate complexation has only been experimentally explored at temperatures up to 70 °C (Götz et al., 2011), with thermodynamic properties only derived from room temperature experiments (Guillaumont et al., 2003). This means that all inferences and models made for elevated temperatures have to date been based on extrapolations of room temperature data. Recent high-temperature experiments on other uranyl complexes have shown that such extrapolations are seldom accurate, often being off by orders of magnitude (Migdisov et al., 2018b; Alcorn et al., 2019; Kalintsev et al., 2019). This casts doubt on the accuracy and relevance of any high-temperature models that explicitly invoke carbonate as a potent transport enabler of uranium.

Considering the ubiquity of carbonate complexation in current uranium transport models, experimental verification of the uranium carrying capacity of high temperature carbonate-bearing fluids is required. Hence, we investigated carbonate's contribution to uranium transport under hydrothermal conditions using a combination of experimental approaches. In-situ spectroscopy experiments using Raman and X-Ray Absorption Spectroscopy (XAS) were conducted to characterize the predominant uranyl complexes present in solution, and autoclave solubility experiments were performed to provide direct insights into the degree to which carbonate enhances the hydrothermal mobility of uranium. Overall, experiments were conducted over a temperature range spanning 100-250 °C - a range permitting to do reliable evaluation of the changes in the behavior of uranium carbonate complexes with temperature. Altogether, these experiments aimed to determine the stoichiometry and thermodynamic properties of the uranyl complexes responsible for uranium's mobility in near-neutral, carbonate-bearing hydrothermal systems.

## **1.2 METHODS**

### **1.2.1 Raman Spectroscopy**

Experiments involved recording of Raman spectra of solutions containing 0.012 m U + 0.1 m NaHCO<sub>3</sub>, which were heated to 50 °C, 75 °C, 98 °C and 146 °C for 16-69 h. Raman spectra were taken at those temperatures, both pre- and post-heating. The spectra were collected using a Horiba Jobin Yvon Evolution Raman spectrometer. The spectrometer is equipped with an 800 mm

focal length, a polarized 532 nm, 250 mW Nd:YAG laser, an edge filter with a Stokes edge of 50  $\text{cm}^{-1}$ , a 1024×256 pixel CCD detector, an 1800 line/mm grating, and a confocal Olympus microprobe with an adjustable slit entry set to 200  $\mu\text{m}$ . All spectra were obtained through a 20× objective lens (SLMPLN, Olympus) using light that was backscattered from the sample.

Expanding on the procedures first developed by Chou et al. (2005), the samples were contained in fused silica capillary tubing (Technical Glass Inc.), inner and outer diameters of 1 mm and 2 mm respectively), which were sealed by a hydrogen-oxygen torch. The capillary tubes were only half filled with liquid sample prior to sealing, and pressure was controlled through equilibrium with the gas phase (i.e. at the saturation vapor pressure of the sample). Temperature control was provided by a Linkam THMS600 stage (Linkam Scientific Instruments) coupled to a T96 temperature controller. In order to provide improved temperature control to the sample, the capillary tubing was housed in a custom-made aluminum heating block, manufactured to sit directly on top of the silver heating stage of the THMS600. This aluminum block is 16 mm in diameter, 20 mm in height, and has a 1 mm channel drilled through it to house the fused silica capillary tubing. Temperature calibration was performed using a K-type thermocouple cemented in a 1×2 mm capillary tube containing air.

### 1.2.2 XAS Experiments

We performed X-ray absorption spectroscopy (XAS) of aqueous solution with  $[\text{UO}_2^{2+}] = 0.05 \text{ m}$  and  $[\text{CO}_3^{2-}] = 0.25 \text{ m}$  (where  $m$  denotes moles of solute per kilogram of water), which was prepared from a 2 mL solution of  $\text{UO}_3 \cdot \text{H}_2\text{O}$  dissolved in  $\text{HClO}_4$  ( $[\text{U}^{6+}] = 0.1 \text{ m}$ ,  $[\text{HClO}_4] = 0.5 \text{ m}$ ) by adding 1.2 mL of 0.5  $m$   $\text{NaOH}$  and 4.2 mL of 0.25  $m$   $\text{NaHCO}_3$ . The spectra were collected at the uranium (U)  $L_{\text{III}}$ -edge (17166.3 eV) at beamline 11-2 at the Stanford Synchrotron Radiation Lightsource (SSRL). We performed these measurements up to 125 °C and 350 MPa using a hydrothermal diamond anvil cell (HDAC) with specially designed radioactive enclosure. The measured sample consists of an aqueous liquid plus vapor bubbles that is placed into the HDAC sample chamber, defined by a 700  $\mu\text{m}$  hole drilled at the center of a 125  $\mu\text{m}$  (100  $\mu\text{m}$  when compressed) thick rhenium (Re) gasket with an outer diameter of 3000  $\mu\text{m}$ . Heating was achieved by resistive heaters near the diamonds, and temperature was measured with K-type thermocouples

attached to each diamond. Pressure was achieved through application of force by tightening screws on the HDAC and, the pressure was estimated based on solution density. Further details about the experimental set-up are described by Dhakal et al., 2019 and Dhakal et al. (2020).

XAS data acquisition in fluorescence mode was made using a 100-element Canberra Ge solid-state monolith detector placed in the standard  $90^\circ$  orientation to the incident X-ray beam. The beam was focused to 250  $\mu\text{m}$  in the horizontal direction and 1 mm in the vertical directions using Kirkpatrick-Baez mirrors and the incident photon energy of the beam was varied using a double-crystal Si (220) monochromator. Detuning of the monochromator crystal was set at 15%. A yttrium (Y) foil in the beam path allowed energy calibration and calibration of XAS spectra to the Y K-edge (17038 eV). The 1<sup>st</sup> derivative with respect to energy of each XAS spectra was calibrated to this edge and data reduction including fitting and subtracting a background function using a pre-edge and post-edge function was performed using the Athena software package (Ravel and Newville, 2005).

### 1.2.3 Solubility Experiments

Solubility experiments were designed to permit the evaluation of both the stoichiometry and formation constants of the predominant uranyl complex responsible for stabilizing uranium in high-temperature carbonate-bearing solutions. Experiments were conducted at 200 and 250°C at saturated water-vapor pressure (SWP) using  $\text{UO}_3$ , which was converted to the reference solid ( $\text{UO}_2(\text{OH})_2$ ) through exposure to experimental solutions and conditions as a reference solid. The experiments that investigated carbonate complexation (Series 1), were set up to have the reference solid interact with solutions containing variable quantities of carbonate added as  $\text{NaHCO}_3$ . In the experiments investigating hydroxyl complexation (Series 2) these solutions instead contained a constant total carbonate concentration which was added as varying ratios of  $\text{NaHCO}_3$  and  $\text{Na}_2\text{CO}_3$  which was used to vary pH. Additionally, to ensure that our chosen activity model was applicable, all solutions also contained 1-2 m NaCl. Uranium is a redox sensitive element with its hexavalent and tetravalent oxidation states being the most common in natural systems. The speciation behaviors of both valence states are significantly different (Guillaumont et al., 2003; Migdisov et al., 2018b; Timofeev et al., 2018), thus, to prevent interference and ensure that experiments were



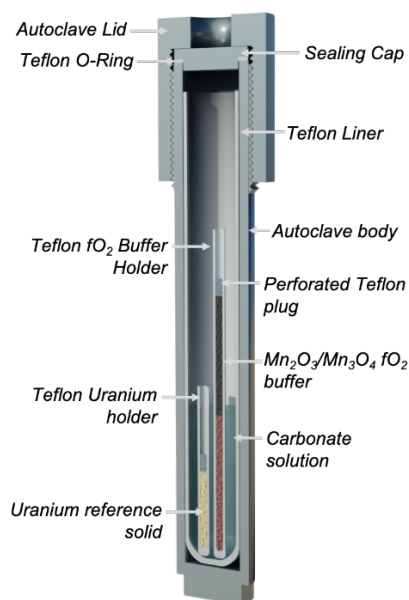


Figure 1.1. Schematic diagram of the autoclave system used for solubility experiments.

only characterizing the solubility and speciation of the hexavalent state a 1:1 Mn<sub>2</sub>O<sub>3</sub>/Mn<sub>3</sub>O<sub>4</sub> mix oxygen fugacity buffer was introduced, which ensured that conditions inside each autoclave remained sufficiently oxidizing to stabilize U(VI) and prevented any U(IV) formation.

In Series 1 experiments, carbonate concentration was varied using NaHCO<sub>3</sub> (Acros Organics, ACS 99.7%) over a range of 0.001 - 0.4 *m*, with care being taken to ensure an ionic predominance of NaCl (Fisher Chemical, Certified ACS) whose concentration was kept at either 1 or 2 *m*. An ionic predominance of NaCl was required in order to permit the usage of the modified extended Debye-Hückel model (Helgeson et al., 1981; Oelkers and Helgeson, 1990; Oelkers and Helgeson, 1991) - activity model details are discussed further below. Based on recent high-temperature experimental data (Migdisov et al., 2018a) thermodynamic calculations suggested that such concentrations of NaCl result in negligible uranyl-chloride species formation at the pH conditions and temperatures investigated. A few solutions were made with higher NaHCO<sub>3</sub> concentrations (up to 0.8 *m*) but their behavior differed little from those with lower concentrations - thus to avoid any precipitation and minimize activity model issues NaHCO<sub>3</sub> concentrations were generally kept below 0.4 *m*. Based on the models for CO<sub>2</sub> solubility in water and NaCl predominated fluids reported by Duan and Sun (2003) such concentrations of carbonate were

stable in solution with outgassing of CO<sub>2</sub> deemed unlikely. In Series 2 experiments, the concentration of carbonate was kept constant at 0.3 m where, based on Series 1 experiments, carbonate complexation was presumed negligible. This carbonate was added as varying ratios of NaHCO<sub>3</sub> and Na<sub>2</sub>CO<sub>3</sub> (Fisher Chemical, Certified ACS, Anhydrous) and was used to both control and buffer pH. Being able to vary pH in such a stable manner allowed us to investigate the relation between pH and uranium solubility, thus permitting the investigation of uranyl hydroxyl speciation. Solution compositions may be found in Table 1.1.

Experiments were conducted using Teflon-lined titanium (Commercial Grade 2) autoclaves into which carbonate-bearing solutions were placed alongside separate small Teflon holders containing the oxygen fugacity buffer and uranium reference solid (as shown in Figure 1.1). Perforated Teflon plugs were placed in all holders to prevent escape of any particulates while still permitting interaction between solid reagents and solution/internal atmosphere. At all times, reagents were solely in contact with Teflon surfaces thus precluding any unexpected chemical interactions between Ti/TiO<sub>2</sub> and reagents. Specific volumes of experimental solution were added such that the holders containing uranium were only submerged at the target experimental temperature via thermal volumetric expansion. The oxygen fugacity buffer holder was made tall enough such that it was never submerged. Loaded autoclaves were initially heated to 150 °C for 2 days to permit equilibration between the oxygen fugacity buffer, the atmosphere within the autoclave and the uranium solid - this ensured that subsequent solution-solid interactions solely involved hexavalent uranium. The experimental solution did not interact with the uranium solid during this pre-heating phase. After this preheating phase, solutions were heated to the target temperature and maintained at such for 5 days to ensure complete equilibration between uranium solids and carbonate solutions (see discussion below). Autoclaves were then extracted and quenched in air to isolate solutions from solids. After opening, both holders were removed and concentrated nitric acid (MilliporeSigma AqueousOmniTrace) was added to the experimental solutions which were then allowed to soak for 24 hours, this was done to dissolve any uranium that may have precipitated during quenching. Solutions were then extracted from autoclaves and uranium concentrations were measured using Inductively Coupled Plasma Mass Spectrometry (ICP-MS) at the Geochemical and Geomaterials Research Laboratories at Los Alamos National Laboratory. A diagram illustrating the key steps of the method is presented in Figure 1.2.

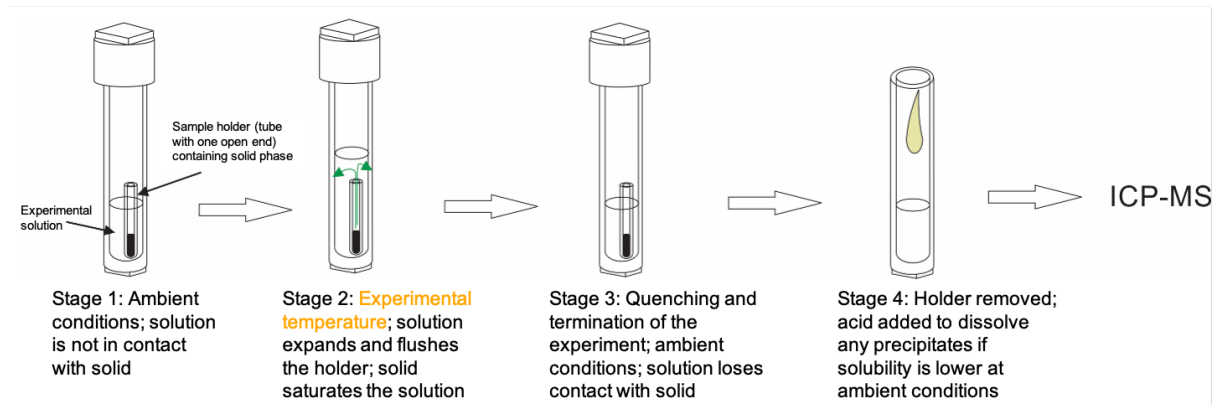


Figure 1.2. Major steps in the autoclave solubility technique.

To ensure the measured concentrations were truly indicative of a state of equilibrium between the reference solid and experimental solution, a series of kinetic experiments were conducted at 200 °C. This temperature was chosen as it represented the lowest temperature investigated using the solubility technique; it was assumed that equilibrium would be achieved over a shorter time period at higher temperatures. A series of autoclaves each containing identical concentrations of NaHCO<sub>3</sub> (0.2 m) were heated to 200 °C after the initial 150 °C ramp period. Individual autoclaves were then periodically extracted and quenched at daily intervals permitting the evaluation of the change in dissolved uranium as a function of time.

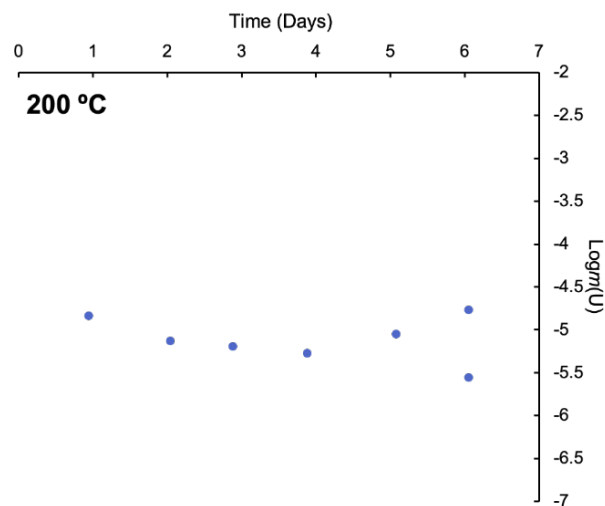


Figure 1.3. Results from the kinetic series conducted at 200°C. Note that equilibrium was essentially reached within 1 day.

Measured uranium concentrations from these kinetic experiments are reported in Figure 1.3 and suggest that equilibrium between the reference solid and experimental solutions was achieved within 1 day - this allowed us to assert that results derived from autoclaves heated for 5 days were truly representative of the equilibrium state between reference solid and solution.

To accurately determine formation constants, a stable reference solid was required. Thermodynamic calculations suggested Paulscherrerite  $\text{UO}_2(\text{OH})_2$  was stable under the chosen experimental conditions. To confirm this, samples of the reference solid were extracted after the experiments were quenched and were characterized using powder X-Ray Diffraction (PXRD). Quantitative phase analysis was performed using the Rietveld method (Hill and Howard, 1987) and confirmed the sole presence of  $\text{UO}_2(\text{OH})_2$ , primarily in its alpha form (~66%) with minor quantities (~33% total) of its beta and gamma polymorphs.

#### 1.2.4 Thermodynamic Calculations

The calculation of solution pH values at temperature and formation constants from experimental data required the activity of all species in solution to be calculated which required a suitable activity model. While there are many such activity models available for ambient conditions, comparatively few are applicable to solutions with appreciable ionic strengths at elevated temperatures. One of the most reliable is the Extended Debye-Hückel equation of state modified for solutions dominated by 1:1 electrolytes (Helgeson et al., 1981; Oelkers and Helgeson, 1990; Oelkers and Helgeson, 1991) (e.g. HCl, NaCl, NaOH) (Equation 1.1).

$$\log \gamma_i = - \frac{A \cdot [Z_i]^2 \cdot \sqrt{I}}{1 + B \cdot \dot{a} \cdot \sqrt{I}} + \Gamma + b_\gamma I \quad (1.1)$$

Where A and B are the Debye-Hückel parameters,  $\gamma_i$ ,  $Z_i$ ,  $\Gamma$  and  $\dot{a}$  are the individual molal activity coefficients, the ionic charge, a molarity to molality conversion factor and ionic size of ion 'i'. The effective ionic strength calculated using the molal scale is I and  $b_\gamma$  is the extended-term parameter for the chosen 1:1 background electrolyte. This necessity for a 1:1 background electrolyte is why all experimental solutions contained 1-2 molal NaCl. Note that Equation 1.1 was only used to

calculate the activity coefficients of charged species whereas the activities of neutral species were calculated using a simplified form of Equation 1 described in Equation 1.2.

$$\log \gamma_i = \Gamma + b_\gamma I \quad (1.2)$$

In all thermodynamic calculations, we defined the experimental system with the following aqueous species:  $H^+$ ,  $OH^-$ ,  $Cl^-$ ,  $HCl^0$ ,  $NaCO_3^-$ ,  $NaHCO_3^0$ ,  $Na^+$ ,  $NaCl^0$ ,  $NaOH^0$ ,  $CO_2^0$ ,  $CO_3^{2-}$ ,  $HCO_3^-$ ,  $UO_2^{2+}$ ,  $UO_2(OH)_2(cr)$ ,  $UO_2Cl^+$ ,  $UO_2Cl_2^0$  using data sourced from Shock et al. (1997), Sverjensky et al. (1997), Tagirov et al. (1997), Miron et al. (2016) and Migdisov et al. (2018b). Data for  $H_2O$  were sourced from the work of Marshall and Franck (1981).

## 1.3 RESULTS

### 1.3.1 Raman Spectroscopy

Our study commenced with a Raman spectroscopy investigation on carbonate-bearing solutions in which appreciable concentrations of uranium were dissolved at ambient conditions. This technique permitted *in situ* observation of uranium's bonding behavior with carbonate at each given temperature (T) and pressure (P) condition. Raman experiments were performed on a solution containing 0.012 *m*  $UO_2^{2+}$  and 0.1 *m*  $NaHCO_3$ . This carbonate concentration was chosen as an intermediate representative of the concentrations found in groundwater and uranium-bearing hydrothermal systems, which altogether typically span a range from 0.001 - 0.2 *m*, though higher concentrations have been suggested for some extreme systems (Cuney, 1978; Hem, 1985). Spectra were collected at 25, 50, 98 and 146 °C at 1 bar or water vapor pressure (whichever was higher), spectra were collected both immediately upon reaching the desired temperature and after 16-67 hours to provide enough time for equilibrium to be reached (Figure 1.4). Although experiments at higher temperatures were planned, they were not performed due to the discovery of precipitation of uranium from solution as will be discussed below. In planning these experiments, it was assumed that, whereas the behavior of uranium in carbonate solutions is well characterized at ambient conditions and has been somewhat evaluated at  $T < 100$  °C (Götz et al., 2011), at temperatures above 100 °C its behavior in such systems was most in need of attention and

experimental verification. At all temperatures, solubility calculations based on thermodynamic properties presented in the PSI Nagra Database (Thoenen et al., 2014) as implemented by GEMS Selektor (Kulik et al., 2013) suggested that all uranium should have remained in solution, predominantly in the form of the uranyl tricarbonate complex,  $[\text{UO}_2(\text{CO}_3)_3]^{4-}$ . These predictions were confirmed by Raman spectroscopy at 25, 50 and 98 °C, with spectra corresponding to uranyl tricarbonate. However, counter to predictions from the theoretical model, at 146 °C we observed a loss of uranyl tricarbonate from solution (Figure 1.5) – this was coupled with an increase in free carbonate and precipitation of a solid uranium phase. Methodological limitations precluded in situ characterization of this phase but by using the same thermodynamic model later used for our subsequent solubility experiments (which omits uranyl carbonate complexes), we determined this phase was likely  $\text{UO}_2(\text{OH})_2(\text{s})$ , though, if added to the model,  $\text{Na}_2\text{U}_2\text{O}_7$  was another possibility. Given that the wide body of prior work discussed above has relied on extrapolations similar to those used in our thermodynamic calculations, these results cast some doubt on the stated capability of carbonate-bearing solutions to carry appreciable concentrations of uranium at temperatures  $\geq 150^\circ\text{C}$ .

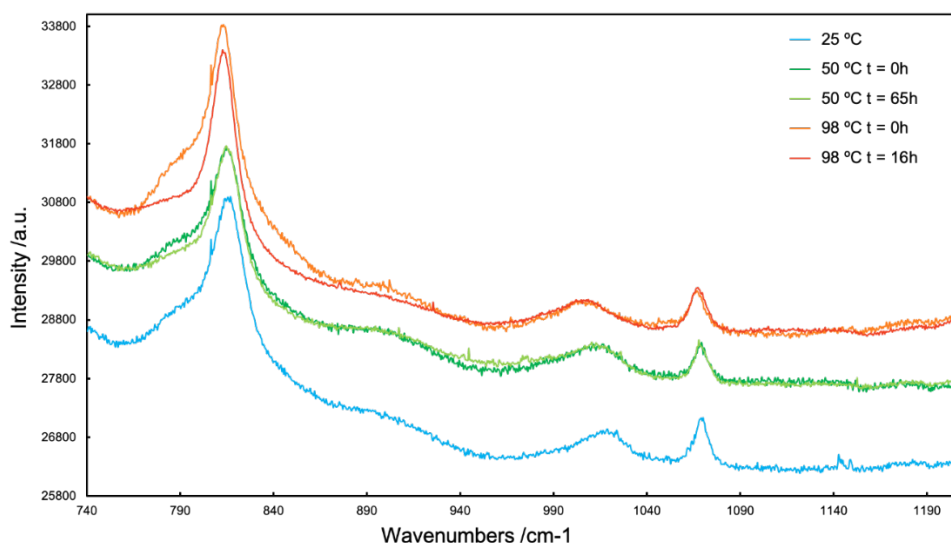


Figure 1.4. Raman spectra of  $0.012\text{ m UO}_2^{2+} + 0.1\text{ m NaHCO}_3$  taken at 25, 50 and 98°C, before and after heating. The spectra show no difference in the aqueous speciation after extended exposure to temperature.

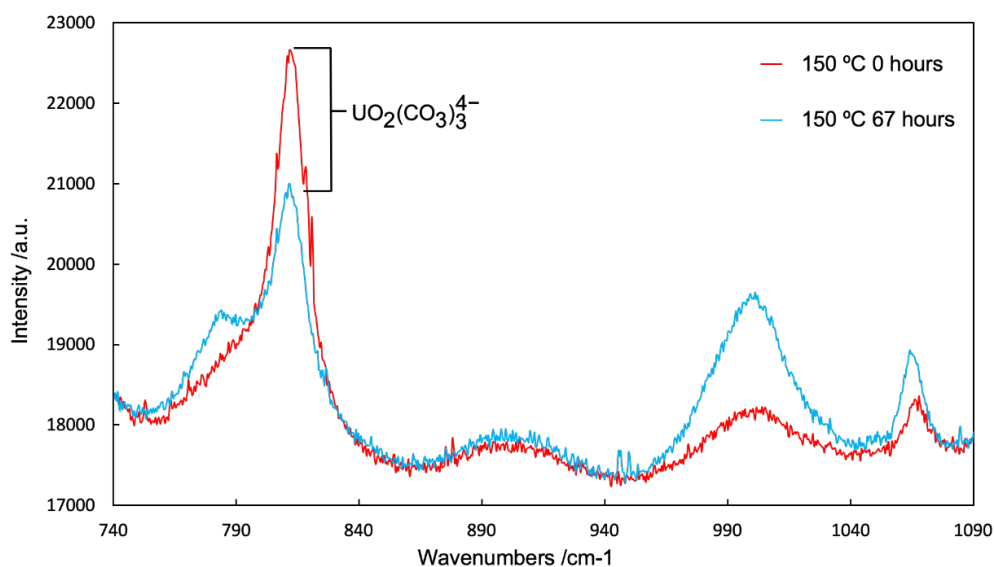


Figure 1.5. Raman Spectra of a solution of 0.012 m  $\text{UO}_2^{2+}$  and 0.1 m  $\text{NaHCO}_3$  collected at 146 °C before and after heating for 67 hours. The U-O v1 stretching mode peak associated with the uranyl tricarbonate complex<sup>32</sup> can be seen in both spectra but has diminished after 67 hours. The broad peak visible in all spectra at ~792 cm-1 corresponds to a water background signal. Peaks at ~1020 cm-1 and ~1070 cm-1 correspond to  $\text{HCO}_3^-/\text{CO}_3^{2-}$  and indicate that carbonate was stable in solution. Note the increase in available carbonate after 67 hours consistent with the breakdown of uranyl tricarbonate complexes.

### 1.3.2 X-Ray Absorption Spectroscopy

To verify the discrepancy between the predicted and observed behavior of uranium in carbonate solutions, we further investigated the molecular level structure of the uranyl species present in the studied aqueous solution by XAS using a Hydrothermal Diamond Anvil Cell (HDAC) (Dhakal et al., 2019; Dhakal et al., 2020). As with the Raman spectroscopy investigation discussed above, the HDAC XAS technique also permitted *in situ* solution characterization at temperatures and pressures of interest.

This experiment was conducted on a solution containing 0.25 m  $\text{NaHCO}_3$  and 0.05 m  $\text{UO}_2^{2+}$ . EXAFS (Extended X-Ray Absorption Fine Structure) spectra and corresponding Fourier transforms are reported in Figure 1.6. Spectra were collected up to 125 °C, and similar to the Raman results, they showed a decrease in the spectral features associated with uranyl carbonate

complexes with increasing temperature. Full fitting of the EXAFS was not performed and instead these paths were used to obtain a qualitative understanding of the coordination chemistry of this

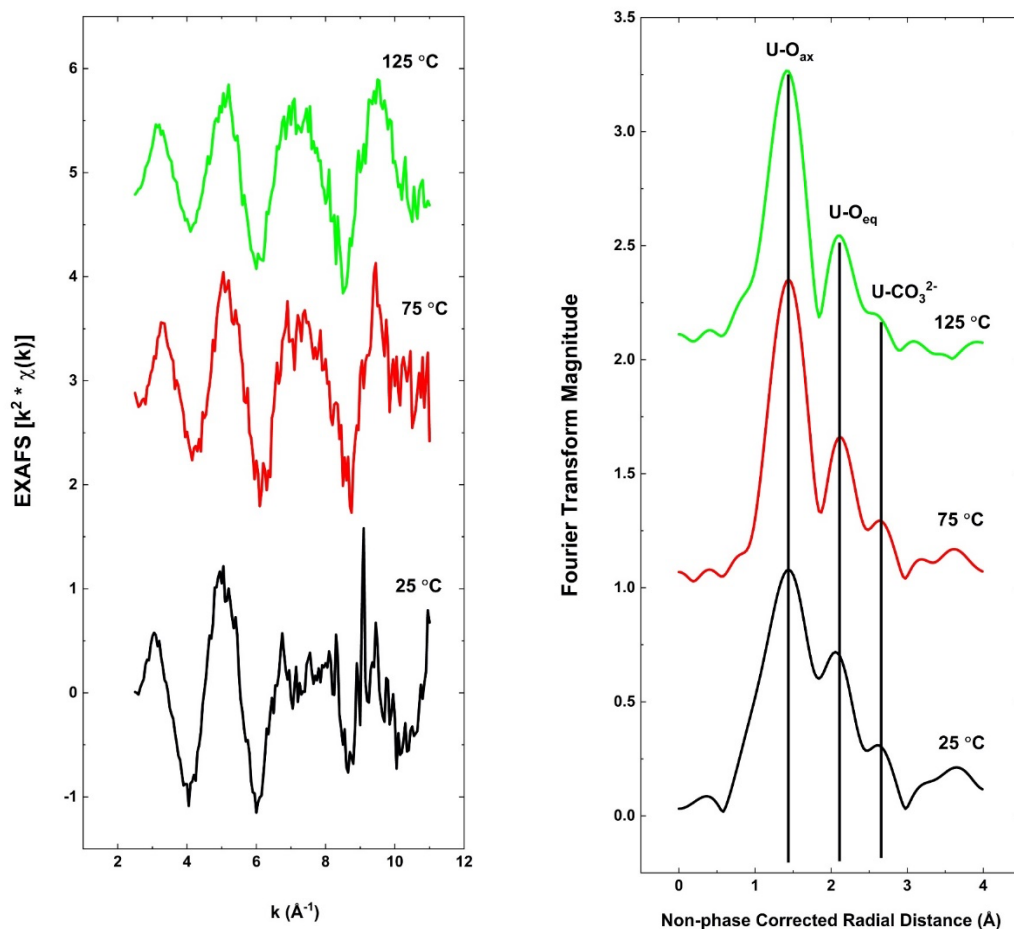


Figure 1.6. (a) U LIII-edge  $k^2$ -weighted EXAFS spectra ( $k = 3.0 - 10.5 \text{ \AA}^{-1}$ ) from 25 °C to 125 °C. (b) Corresponding Fourier transform of EXAFS spectra. Three main features are observable corresponding to single-scattering paths with respect to the uranium absorber atom and two axial oxygen ( $\text{O}_{\text{ax}}$ ) atoms, a variable number of equatorial oxygen ( $\text{O}_{\text{eq}}$ ) atoms, and a variable number of carbon atoms ( $\text{U-CO}_3^{2-}$ ). With increasing temperature, the intensity corresponding to the  $\text{U-CO}_3^{2-}$  scattering path decreases indicating a loss of carbonate complexation. Note the diminishment, with increasing temperature, of the peak associated with the uranium-C single scattering path at  $\sim 2.6 \text{ \AA}$  and the peaks between 3-4  $\text{\AA}$  typically attributed to multiple scattering paths associated with the carbonate anion.

solution. Two main peaks are observable in the FT data (Figure 1.6b), which arise due to single-scattering paths corresponding to two axial oxygen atoms, a variable number of equatorial oxygen atoms (6 in the case of the uranyl tricarbonate complex at ambient pressure and temperature). The



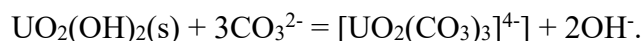
axial oxygen atoms correspond to the oxygen atoms of the  $\text{UO}_2^{2+}$  cation and the equatorial oxygen atoms are from the  $\text{CO}_3^{2-}$  and  $\text{H}_2\text{O}$  molecules that coordinate around the equator of the  $\text{UO}_2^{2+}$  ion. A third peak manifesting as a shoulder to the right of the  $\text{O}_{\text{eq}}$  peak, represents the contribution due to single scattering with the carbon atoms (i.e., U - C single scattering) associated with  $\text{CO}_3^{2-}$  ligands. As temperature increases, a clear decrease in the intensity of this shoulder is observed, indicating a potential reduction in  $\text{CO}_3^{2-}$  complexation at elevated temperatures.

By 125 °C, the intensity of this feature was minimal. Also of note is a general decrease in the intensity of the FT spectra with increasing temperatures potentially linked to changing complexation of the system. The XAS data strongly suggest that carbonate complexes of uranium, being predominant at lower temperatures (which can be clearly seen from the U- $\text{CO}_3$  feature on the spectra collected at  $T < 100$  °C), effectively disappear from the solution when temperature exceeds 100-120 °C, leading to a drastic decrease in the ability of carbonate-bearing solutions to transport uranium.

### 1.3.3 Solubility Experiments

The unexpected and drastic changes in the behavior of uranium in high temperature carbonate-bearing solutions from our spectroscopic analyses represent a major finding which significantly alters our understanding of the behavior of uranium in hydrothermal systems. Unfortunately, such behavior precluded any further spectroscopic experiments at higher temperatures as the quantities of uranium that remained in solution were below the detection limits of both *in situ* Raman and XAS techniques. Thus, to perform a cross-check of these spectroscopic observations and to determine whether this unexpected behavior is present at temperatures above 150 °C, autoclave solubility experiments were also conducted. Solubility experiments involve determination of the solubility of solid phases in solutions of interest. In the case of our experiments, we investigated the ability of carbonate-bearing solutions (up to 0.8 m) to dissolve uranyl hydroxide ( $\text{UO}_2(\text{OH})_2(\text{s})$ ). This phase was determined to be stable at the investigated P,T conditions and solution compositions by both thermodynamic modelling and post-experiment X-Ray Diffraction (XRD) measurements of the solids used. This technique takes advantage of being able to measure the change in U solubility as a function of ligand concentration - in this case

carbonate ( $\text{CO}_3^{2-}$ ). For example, if uranium in solution were predominantly present as  $[\text{UO}_2(\text{CO}_3)_3]^{4-}$ , the primary equation describing its solubility would be:



Based on the associated equilibrium constant, the uranium concentration will increase by 3 orders of magnitude if carbonate concentration increases by one order of magnitude (slope of 3 on a log activity of uranium complex vs log activity of carbonate ion plot). By measuring this relationship, these experiments would determine if  $\text{UO}_2(\text{OH})_2$  solubility was in any way correlated to the presence of carbonate in high-T solutions as well as permit the evaluation of the stoichiometry and thermodynamic molal properties of the predominant uranyl complex controlling solubility.

Compositions of solutions from both experimental solubility series are reported in Table 1.1 along with recorded uranium solubilities, calculated pHs at the experimental temperature and pH corrected uranium concentrations. Results from these experiments, collected at 200 and 250 °C and saturated water-vapor pressure are summarized in Figure 1.7 and are reported alongside predicted values of uranium solubility under the same conditions using data from the PSI Nagra Thermodynamic Database as implemented by GEMS Selektor (Kulik et al., 2013; Thoenen et al., 2014). It should be noted that the calculated solubilities we report merely present one potential result of room temperature extrapolations. A similar attempt was made by Bastrakov et al. (2010) however the formation constants derived in their work suggested even greater stability of uranyl carbonate complexes at temperature – as such, relative to their results, our calculations show a potential minimum in the degree of accuracy one might expect using current room temperature data and extrapolation techniques.

Table 1.1. Compositions and results from all autoclave solubility solutions. All concentrations are reported as mol/kg of H<sub>2</sub>O. pH values were calculated for the experimental temperature using the modified extended Debye Hückel model - system definition and thermodynamic molal property details are discussed further below. pH corrected values were normalized to a pH of 8 and were made based on a 1:1 dependence of log uranium concentration on pH as suggested by results reported in Figure 1.4 in the main text.

$T$ (°C)	[NaCl]	[NaHCO <sub>3</sub> ]	[Na <sub>2</sub> CO <sub>3</sub> ]	log $m$ (U)	pH <sub>r</sub>	Log $m$ (U) (pH norm)
200	1	0.02	0	-5.09	7.81	-5.28
200	1	0.01	0	-5.10	7.69	-5.41
200	1	0.02	0	-5.95	7.81	-6.14
200	1	0.05	0	-5.95	7.95	-6.01
200	1	0.1	0	-5.84	8.01	-5.82
200	1	0.200	0	-5.44	8.05	-5.39
200	1	0.010	0	-4.56	7.69	-4.87
200	1	0.010	0	-4.96	7.69	-5.27
200	1	0.100	0	-5.24	8.01	-5.22
200	1	0.100	0	-5.33	8.01	-5.32
200	1	0.1	0	-4.58	8.01	-4.56
200	2	0.05	0	-5.44	7.84	-5.60
200	2	0.1	0	-4.80	7.92	-4.88
200	2	0.15	0	-4.59	7.95	-4.64
200	2	0.3	0	-4.51	7.98	-4.52
200	1	0.2	0	-4.83	8.06	-4.77
200	1	0.2	0	-5.13	8.06	-5.06
200	1	0.2	0	-5.19	8.06	-5.13
200	1	0.2	0	-5.27	8.06	-5.21
200	1	0.2	0	-5.05	8.06	-4.99
200	1	0.2	0	-4.76	8.06	-4.70
200	1	0.2	0	-5.55	8.06	-5.49
200	2	0	0.3	-6.98	9.78	-5.19
200	2	0.1	0.2	-7.58	9.51	-6.06
200	2	0.1	0.2	-8.21	9.51	-6.70
200	2	0.15	0.15	-7.69	9.34	-6.35

---

200	2	0.15	0.15	-7.490	9.34	-6.15
200	2	0.2	0.1	-6.74	9.12	-5.62
200	2	0	0.1	-6.82	9.49	-5.33
200	2	0	0.2	-6.95	9.68	-5.28
200	2	0	0.3	-8.39	9.78	-6.61
200	2	0	0.4	-7.13	9.85	-5.28
200	2	0	0.5	-6.53	9.91	-4.63
250	1	0.001	0	-4.69	7.22	-5.47
250	1	0.005	0	-4.79	7.63	-5.16
250	1	0.01	0	-6.34	7.79	-6.55
250	1	0.03	0	-5.67	8.02	-5.65
250	1	0.05	0	-5.94	8.12	-5.82
250	1	0.08	0	-6.68	8.20	-6.48
250	1	0.1	0	-6.08	8.23	-5.85
250	1	0.001	0	-6.15	7.22	-6.93
250	1	0.005	0	-6.94	7.63	-7.32
250	1	0.01	0	-6.95	7.79	-7.17
250	1	0.1	0	-7.17	8.23	-6.94
250	1	0.2	0	-5.72	8.32	-5.40
250	1	0.3	0	-5.81	8.35	-5.46
250	1	0.4	0	-6.94	8.37	-6.57
250	2	0.2	0	-6.76	8.20	-6.56
250	2	0.4	0	-7.36	8.27	-7.09
250	2	0.5	0	-6.87	8.28	-6.59
250	2	0.6	0	-7.42	8.29	-7.13
250	2	0.65	0	-7.67	8.30	-7.37
250	2	0.7	0	-7.04	8.30	-6.74
250	2	0.75	0	-7.42	8.30	-7.18
250	2	0.8	0	-6.55	8.30	-6.25
250	2	0.1	0.2	-7.39	9.52	-5.87
250	2	0.1	0.2	-7.32	9.52	-5.80
250	2	0.15	0.15	-6.87	9.38	-5.49
250	2	0.2	0.1	-7.34	9.20	-6.15
250	2	0.2	0.1	-7.57	9.20	-6.37
250	2	0.3	0	-6.39	8.25	-6.15

---

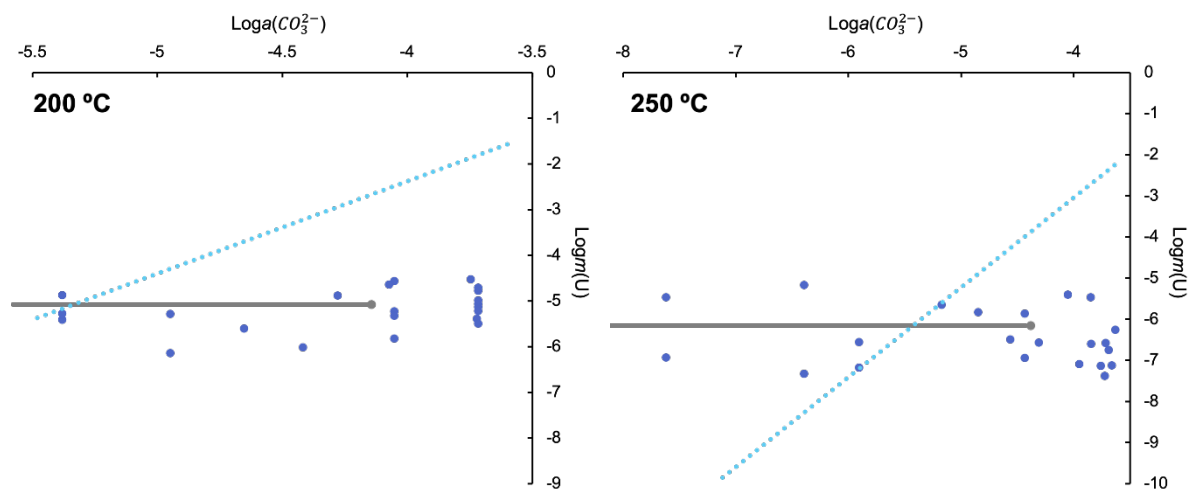


Figure 1.7. Measured and calculated solubilities of  $\text{UO}_2(\text{OH})_2$  as functions of calculated carbonate activity. Measured solubilities are shown as dark blue points and calculated solubilities for the same system are shown in light blue. A gradient of 3 for the calculated solubilities would suggest a predominance of the  $\text{UO}_2\text{CO}_3^{4-}$  complex, which, however, is not the case as revealed by the experimental results. The dark grey line delineates a range of carbonate activities for groundwater and uranium-bearing hydrothermal systems. Note that data spreads spanning an order of magnitude are typical for autoclave solubility experiments.

In stark contrast to theoretical predications, our data suggest that carbonate has no systematic effect on enhancing the solubility of uranium at elevated temperatures, and that the total solubility of uranium in carbonate-bearing solutions is significantly lower than expected - indeed, discrepancies of up to 4 orders of magnitude are observed between theory and our experiments. Thus, these results confirm observations made using Raman and XAS techniques, altogether suggesting that uranium-carbonate complexes do not have any detectable contribution to the mass balance of dissolved uranium at the investigated experimental conditions. It should be emphasized that the experimental conditions (both with regards to carbonate concentrations and temperatures) investigated are indeed relevant to a number of natural and engineered (e.g. nuclear waste repository associated) uranium-bearing hydrothermal systems. The findings reported above cast serious doubt on any models of high-temperature aqueous uranium movement that invoke carbonate as a transporting ligand - indeed, such models may be overestimating the mobility of uranium in hydrothermal systems by several orders of magnitude. Our spectroscopic and solubility data suggest that carbonate cannot be invoked as a transporting agent for uranium in ore deposits

nor as a mobility enabler of uranium from nuclear waste in repositories at their peak thermal conditions (at least proximally to the waste itself). Indeed, the carbonate ion should only be

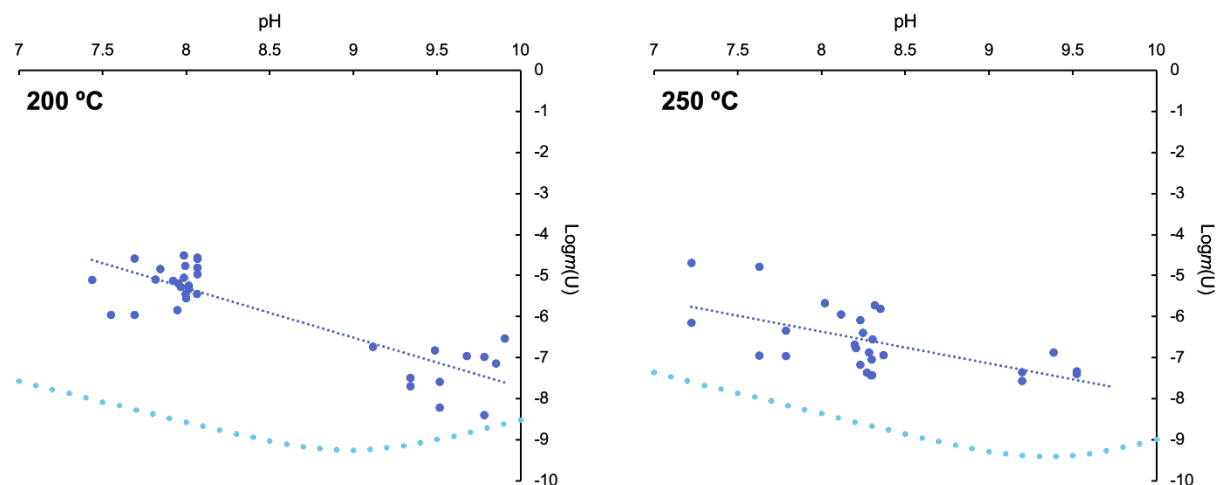


Figure 1.8. Measured and calculated solubilities of  $UO_2(OH)_2$  plotted as functions of pH at temperature. Measured solubilities and trend line are shown in dark blue. Calculated solubilities (assuming no uranyl carbonate speciation) are shown in light blue. Calculated solubilities suggest a predominance of  $UO_2OH^+$  over most of the pH range shown with a shift towards  $UO_2(OH)_{2(aq)}$  then  $UO_2(OH)_3^-$  predominates at pH values  $>\sim 9.5$  as indicated by gradients of 0 and 1 consistent with the reactions  $[UO_2(OH)_2(s) = UO_2(OH)_{2(aq)}]$  and  $[UO_2(OH)_{2(s)} + H_2O = UO_2(OH)_3^- + H^+]$ .

considered as a relevant transport enhancer of uranium in natural waters at temperatures below 100 °C.

A major question that arises in the context of our results is, if carbonate is ineffective at enhancing the mobility of uranium at temperatures above 100 °C, what complexes are instead responsible for uranium transport under such conditions? Furthermore, are these complexes more or less stable than theoretically predicted? At room temperature, the next most important group of complexes responsible for uranium transport in near-neutral fluids are the hydroxyl ( $OH^-$ ) complexes and extrapolations suggest that this is also true at elevated temperatures (Guillaumont et al., 2003; Skirrow, 2009; Bastrakov et al., 2010). However, such extrapolations are solely based on low temperature (25-85°C) experimental data (Zanonato et al., 2004) which, as already illustrated can lead to dubious predictions. To investigate this alternative, we performed another set of solubility experiments - this time maintaining a constant carbonate concentration (0.3 m - which based on the results reported in Figure 1.3 was presumed to have no effect on uranium solubility) and varying pH. Solution pH was controlled by varying relative ratios of  $NaHCO_3$  and

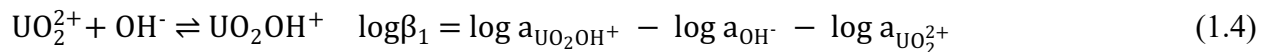
Na<sub>2</sub>CO<sub>3</sub>, yielding a pH range from ~7-10. The results from this new set of experiments are reported in Figure 1.8. Again, we have plotted theoretically calculated values for uranium solubility alongside our experimental results. These calculations assumed no contribution of carbonate speciation to the mass balance of dissolved uranium, with hydroxyl complexes instead being invoked as the primary control on uranium solubility.

When plotted against pH, the uranium concentrations observed in our experiments show a dependence (gradients of -1.2 and -0.77 at 200 °C and 250 °C, respectively) that suggests the predominance of the UO<sub>2</sub>OH<sup>+</sup> complex consistent with the reaction described in Equation 1.3:



Furthermore, discrepancies between theoretically calculated uranium solubilities range from about 1-3 orders of magnitude suggesting that the extrapolations of [UO<sub>2</sub>OH<sup>+</sup>] molal properties from 85 °C (Zanonato et al., 2004) are qualitatively valid but require quantitative revision.

To derive the Gibbs free energy of formation of UO<sub>2</sub>OH<sup>+</sup> at both 200 and 250 °C the OptimA program (part of the HCh software package) was utilized. This required a chemical system definition and activity model, both of which we have described above. Through a least-squares optimization procedure (i.e. minimizing deviation between experimental and measured values of uranium solubility by varying the Gibbs free energy of the UO<sub>2</sub>OH<sup>+</sup> complex), OptimA was used to derive the Gibbs free energies of formation of UO<sub>2</sub>OH<sup>+</sup> as well as the uncertainty of this parameter at both 200 and 250 °C. These Gibbs free energies were then used to calculate formation constants (logβ<sub>1</sub>) for Equation 1.4 at those temperatures. Derived formation constants are reported in Table 1.2 alongside formation constants for the same reaction reported up to 85 °C by Zanonato et al. (2004).



To permit the interpolation of the formation constants for Equation 1.4, all values reported in Table 1.2 have been fitted to the modified Ryzhenko-Bryzgalin (MRB) model (Ryzhenko et al., 1985) using the OptimC program (also a part of the HCh software package).

$$\log K_{(T,P)} = \frac{T_r}{T} \log K_{(T_r,P_r)} + B_{(T,P)} * \left( A_{zz/a} + \frac{B_{zz/a}}{T} \right) \quad (1.5)$$

K is the dissociation constant of the ion pair and  $T_r$  and  $P_r$  refer to the reference temperature and pressure conditions.  $B_{(T,P)}$  accounts for changes in the properties of water with pressure and temperature and is calculated using values from (Marshall and Franck, 1981).  $A_{zz/a}$  and  $B_{zz/a}$  are both empirical parameters derived by fitting experimental data to the model. Using these newly derived parameters (Table 1.3), we have tabulated new formation constants for Equation 1.4 from 25 to 250 °C, these are reported in Table 1.4.

Table 1.2. Formation constants for Equation 1.4.

Temperature (°C)	25 <sup>a</sup>	40 <sup>a</sup>	55 <sup>a</sup>	70 <sup>a</sup>	85 <sup>a</sup>	200 <sup>b</sup>	250 <sup>b</sup>
$\log \beta_1$	8.60	8.62	8.27	8.50	8.49	11.81	11.33
Uncertainty	±0.24	±0.11	±0.24	±0.11	±0.15	±0.52	±0.57

<sup>a</sup>Values reported by Zanonato et al. (2004). <sup>b</sup>Values derived in this work.

Table 1.3. MRB fitting parameters for the  $UO_2OH^+$  dissociation reaction using values reported in Table 1.2.

Species	pK(298)	A(zz/a)	B(zz/a)
$UO_2OH^+$	8.334	2.279	-7.47

Table 1.4. Formation constants of Equation 1.4 at a range of temperatures calculated using MRB parameters reported in Table 1.3.

T (°C)	$\log \beta_1$
25	8.33
50	8.50
75	8.76
100	9.08
125	9.44
150	9.85
175	10.29
200	10.78
225	11.33
250	11.96



## 1.4 DISCUSSION

From the combination of Raman, XAS and solubility results presented above, it is evident that carbonate complexes are irrelevant at temperatures above 100 °C, and that the capability of carbonate to mobilize uranium under hydrothermal conditions has historically been greatly overestimated. As exemplified by the recent work of Ewing (2015), uranyl-carbonate complexation has often been cited as a primary concern for waste repository design largely due to its ubiquity and potency at room temperature conditions (Clark et al., 1995; Ewing, 2015; Runde, 2015). At thermal maximum, temperatures within the vicinity of stored high-level radioactive waste may span from 100-250°C (Johnson et al., 2002; Buscheck et al., 2003; Haukwa et al., 2003; Zhou et al., 2010; Greenberg et al., 2013; Blanco Martín et al., 2015; Hardin et al., 2015) though naturally this is dependent on repository design. At such temperatures, uranyl-carbonate complexation is suppressed and our results additionally indicate that  $\text{UO}_2\text{OH}^+$  becomes less stable with increasing temperature leading to the rather counterintuitive conclusion that high temperatures may in fact stifle uranium liberation and transport from nuclear waste and that the risk of liberation increases as the waste cools and uranyl-carbonate complexes become relevant. Naturally we do not suggest that all repositories should be maintained at elevated temperatures but this conclusion suggests that in terms of carbonate-bearing solutions greater care should be considered to the later, cooler stages of a repository's life when uranium transport by carbonate-bearing fluids becomes enhanced.

## 1.5 CONCLUSION

To conclude, results from the experiments reported here suggest that at temperatures above 150 °C the uranium carrying capacity of carbonate-bearing fluids relevant to radioactive waste repositories may have been historically overstated. We have demonstrated that at such conditions carbonate is incapable of enhancing uranium mobility which suggests that a significant number of uranium transport models may require revisiting and revision. On the other hand, we have also found that the carrying capacity of uranyl hydroxy complexes is significantly higher than

historically believed and that they could potentially account for a significant portion of the uranium carrying capacity of a wide range of natural solutions.

## **2. THERMODYNAMIC PROPERTIES OF URANYL-CHLORIDE AND URANYL-SULFATE AQUEOUS COMPLEXES AT ELEVATED TEMPERATURES**

## 2.1 INTRODUCTION

The Spent Fuel and Waste Disposition (SFWD) program supports R&D efforts focused on re-visiting and refining thermodynamic data for aqueous complexes that can control or contribute to Spent Fuel (SF) degradation processes at elevated temperatures. Considering that uranium is the main component of SF, the speciation of U in hydrothermal solutions and adequacy of existing high temperature thermodynamic data (most of which were derived by theoretically extrapolating from low temperature values) is of main interest. As discussed in Part 1 of this report, the most common ligands controlling the mobility of U in natural hydrothermal solutions are  $\text{Cl}^-$ ,  $\text{SO}_4^{2-}$ ,  $\text{OH}^-$ , and  $\text{CO}_3^{2-}$ . Since 2018,  $\text{UO}_2^{2+}/\text{Cl}^-$  and  $\text{UO}_2^{2+}/\text{SO}_4^{2-}$  chemical systems have been re-visited at temperatures up to 250 °C. The data were published in *Geochimica et Cosmochimica Acta* and *J. Phys. Chem. B* (Migdisov et al., 2018a; Alcorn et al., 2019; Kalintsev et al., 2019) and demonstrate appreciable deviation from predictions made based on low temperature data (see previous reports and publications cited above). Thus, the aim of the work presented in this report is to summarize and consolidate the current data, and present stability constants/Gibbs free energies of the determined aqueous species in the form of parameters of equation of states most commonly used in the literature and modelling software.

## 2.2 DATA REPRESENTATION, EOS FORMULATIONS AND DATA FITTING

The data presented in this report are divided into two appendixes devoted to the different chemical systems investigated:  $\text{UO}_2^{2+}/\text{Cl}^-$  and  $\text{UO}_2^{2+}/\text{SO}_4^{2-}$ . Each appendix presents tables listing the source experimental data (formation pK) taken into consideration, the derived parameters for the Modified Ryzhenko-Bryzgalin interpolative EoS, the optimized/interpolated values of formation pK, and the error characterizing the quality of the fit. Also included are tables with summarized MRB parameters for each aqueous species discussed, and tables with the Helgeson-Kirkham-Flowers (HKF) parameters for each species derived using the PRONSPREP97 code, whose values were used as initial guesses for further refinement based on the experimental data. In addition, details of the HKF fit performed based on the tabulated Gibbs free energies are

included, which list the errors associated with the fit quality and additional constraints used for the optimization. Tables summarizing the final recommended values of the HKF EoS for each species discussed in this report are also listed. Finally, formation constants for each species of interest, tabulated at a range of T and P conditions, are reported.

The Modified Ryzhenko-Bryzgalin EoS (Ryzhenko et al., 1985) is a model that has been developed to predict equilibrium constants for ion-association reactions of the type:



The model expresses Gibbs free energies of ion-association reactions as a sum of electrostatic and non-electrostatic terms.

$$\Delta_r G = \Delta_r G^{non-electr.} + \Delta_r G^{electr.} . \quad (2.2)$$

An important limitation of this model is the assumption that in the case of ionic species, electrostatic forces play the major role in interactions, whereas the non-electrostatic term is suggested to be temperature- and pressure-independent. Hence, equation (2.2) is expressed as:

$$\Delta_r G = \Delta_r G^{non-electr.} + \frac{|z^+ z^-| e^2 N}{(r_A + r_B) \varepsilon} \quad (2.3)$$

where,  $e$  is the electron charge,  $N$  is the Avogadro number,  $\varepsilon$  is the dielectric constant of water at T and P, and  $r_A + r_B = a$  is the sum of radii of associating ions. The final EoS for the MRB model is expressed in the form of pK for association constants:

$$pK^{T,P} = \frac{298.15}{T} pK^{298,1 \text{ bar}} + \frac{72600 |z^+ z^-|}{T a} \left( \frac{1}{\varepsilon_{T,P}} - 0.0128 \right) \quad (2.4)$$

or

$$pK^{T,P} = \frac{298.15}{T} pK^{298,1 \text{ bar}} + \theta^{T,P} \left( \frac{|zz|}{a} \right)_{eff} \quad (2.5)$$

where,  $\left( \frac{|zz|}{a} \right)_{eff} = A + \frac{B}{T}$ , with  $A$  and  $B$  to be adjustable parameters for each given association reaction, and  $\theta^{T,P}$  is the reaction-independent parameter computed from the dissociation constant of water according to Marshall and Franck (1981). The value of  $\left( \frac{|zz|}{a} \right)_{eff}$  for water employed in the model is set at 1.0107. As shown in the equation (2.5), the model employs only 3 adjustable parameters, namely  $pK^{298,1 \text{ bar}}$ ,  $A$ , and  $B$ , and, thus, formation constants experimentally determined

at a range of temperatures for ion-associating aqueous species can be reliably fitted to the model using the least squares regression or other search algorithms. The MRB model has proven to be reliable for interpolating experimental data as a function of temperature (e.g., Liu et al., 2012; Timofeev et al., 2015; Nisbet et al., 2021), however, due to over-simplifications on the basis of the model, it is questionable for any type of long-range temperature extrapolations, and therefore, the latter case should be used with extreme caution. The data treatment presented in this report therefore uses the MRB for data interpolation only.

The HKF model is based on the Born model (Born, 1920), which defines the energy required for the removal of an ion from a vacuum to a solvent:

$$\Delta G_S^0 = \omega \left( \frac{1}{\varepsilon} - 1 \right) \quad (2.6)$$

where  $\omega$  is the conventional Born parameter  $\omega = \frac{N_a z^2}{2r} - \left( \frac{N_a z_{H^+}^2}{2r_{H^+}} \right) z = \frac{N_a z^2}{2r} - 0.5387z$ , where  $N_a$  is the Avogadro's number,  $z$  is the charge of the ion,  $r$  is the radius of the ion, and  $\varepsilon$  is the dielectric constant of the solvent. However, the conventional Born model does not account for the energy required to disrupt the hydrogen bonding network present in the solution, whereby the HKF model modifies it by introducing the concept of effective electrostatic radii of ions ( $r_e$ ):

$$\omega = \omega^{abs} - 0.5387z; \quad \omega^{abs} = \frac{\eta z^2}{r_e} \text{ where } \eta = 1.66027 \cdot 10^5 \text{ } \AA \text{ cal mol} \quad (2.7)$$

$r_e = r_x + |z|(k_z + g(T, P))$ , where  $r_x$  is the crystallographic radius,  $k_z = 0.94 \text{ } \AA$  for cations and is 0 for anions, and  $g(T, P)$  is the solvent function derived by the authors (for more details see (Shock and Helgeson, 1988; Shock et al., 1992; Pokrovskii and Helgeson, 1997; Shock et al., 1997a; Sverjensky et al., 1997)). The HKF model splits the thermodynamic functions which characterize individual ions and complexes by solvation (Born) and non-solvation terms. The non-solvation terms were expressed as follows:

$$\text{For partial molar volumes: } \Delta V_{ns} = a_1 + a_2 f(P) + a_3 f_1(T) + a_4 f(P) f_1(T) \quad (2.8)$$

$$\text{For heat capacities: } \Delta C_{p,ns} = c_1 + c_2 f_2(T) \quad (2.9)$$

$$f_1(T) = \frac{1}{T-\theta}; \quad f_2(T) = \frac{1}{(T-\theta)^2}; \quad f(P) = \frac{1}{\Psi+P} \quad (2.10)$$

where  $a_1, a_2, a_3, a_4, c_1, c_2$  are species-specific adjustable parameters and  $\Theta = 228$  K,  $\Psi = 2600$  bar are the empiric constants. Summarizing the Born and non-solvation terms, the consolidated equations are:

$$\Delta C_P^o = c_1 + \frac{c_2}{(T-\theta)^2} + \omega T \left( \frac{\partial}{\partial T} \left( \frac{1}{\varepsilon^2} \cdot \frac{\partial \varepsilon}{\partial T} \right) \right)_P \quad (2.11)$$

$$\Delta V^o = a_1 + \frac{a_2}{\Psi+P} + \left( a_3 + \frac{a_4}{\Psi+P} \right) \left( \frac{1}{T-\theta} \right) - \frac{\omega}{\varepsilon^2} \left( \frac{\partial \varepsilon}{\partial T} \right)_T \quad (2.12)$$

$$\begin{aligned} \Delta G_{T,P}^o &= \Delta G_{298}^o - S_{298}^o(T - 298.15) - c_1 \left( T \cdot \ln \frac{T}{298.15} - T + 298.15 \right) + a_1(P - 1) + \\ &a_2 \ln \left( \frac{\Psi+P}{\Psi+1} \right) - c_2 \left\{ \left[ \left( \frac{1}{T-\theta} \right) - \left( \frac{1}{298.15-\theta} \right) \right] \left( \frac{\theta-T}{\theta} \right) - \frac{T}{\theta^2} \ln \left( \frac{298.15(T-\theta)}{T(298.15-\theta)} \right) \right\} + \left( \frac{1}{T-\theta} \right) \left( a_3(P - 1) + \right. \\ &\left. a_4 \ln \left( \frac{\Psi+P}{\Psi+1} \right) \right) + \omega \left( \frac{1}{\varepsilon} - 1 \right) - \omega_{298} \left( \frac{1}{\varepsilon_{298}} - 1 \right) + \omega_{298}(T - 298.15) \frac{\partial}{\partial T} \left( \frac{1}{\varepsilon} - 1 \right). \end{aligned} \quad (2.13)$$

Although more accurate and of much higher predictive power than the MRB EoS, the HKF EoS is a multi-parametric model with a large number of species-specific parameters:  $\Delta G_{298}^o, S_{298}^o, c_1, c_2, a_1, a_2, a_3, a_4, \omega$ . The derivation of this many parameters requires either an extremely large experimental dataset, or additional constraints which would link these parameters through empirical or theoretical correlations. These empirical correlations were derived by the HKF developers based on a large number of chemical systems previously studied (Sverjensky et al., 1997). Among these correlations is:

$$\omega_{P_r T_r} = -1514.4 S_{P_r T_r}^o + \beta_z, \quad (2.14)$$

where  $S_{P_r T_r}^o$  is in cal mole<sup>-1</sup> K<sup>-1</sup>, and  $\beta_z$  (x10<sup>-5</sup>) = 0.5512, 1.0586, 1.5795, -1.6295, and 3.2120 for species having charges of 1, 2, 3, -1, and -2, respectively. The value of  $\beta_z$  (x10<sup>-5</sup>) for neutrally charged species was estimated to be 0 for volatile species and 0.34 for non-volatile species. Additional correlations are associated with the parameters of the equations of state for partial molar volumes and heat capacity:

$$a_1 = 0.013684 \Delta V_{n,P_r,T_r}^o + 0.1765; \quad a_4 = -4.134 a_2 - 27790; \quad c_2 = 2037 C_{P_r,T_r}^o - 30460 \quad (2.15)$$

The data discussed in this report were first fit to the MRB model, which was used to interpolate and tabulate the formation constants for each species of interest within the experimentally investigated temperature range. The optimization of the adjustable parameters, A and B, provided in this report was performed using the Optim C code (Shvarov, 2015), which

employs the least squares fitting algorithm. Formation constants were tabulated for 20 to 25 °C increments; these values, together with data from Johnson et al. (1992) and Shock et al. (1997) for  $\text{UO}_2^{2+}$ ,  $\text{U}^{4+}$ ,  $\text{Cl}^-$ , and  $\text{SO}_4^{2-}$ , were used to derive apparent Gibbs free energies of formation of the species for the tabulated temperatures.

These apparent Gibbs free energies of formation were then used to derive the HKF EoS parameters. The initial guesses for this derivation were the parameters theoretically predicted by the PRONSPREP97 code (Sverjensky et al., 1997). This code predicts the HKF parameters based on the species standard Gibbs free energies of formation (formation constants for the species determined at 25 °C), and accounts for Eq.2.14-2.15 relationships. These initial estimates were then refined using the temperature dependencies of the species apparent Gibbs free energies obtained at the previous stage (the MRB interpolation). Optimization was performed using the Optim B code (Shvarov, 2015), which, similar to the Optim C code mentioned above, employs the least squares fitting algorithm. Considering that the available experimental data do not provide significant variability in pressure conditions, the parameters of the HKF EoS associated with the characterization of the species partial molar volume (Eq 2.12; parameters  $a_1$ - $a_4$ ) were not optimized and were taken directly from the predictions of PRONSPREP97. The parameters optimized were  $\Delta G_{298}^o$ ,  $S_{298}^o$ ,  $c_1$ ,  $c_2$ , and  $\omega$ . The optimization accounted for correlations described in Equations 2.14-2.15.

### 2.3 ACKNOWLEDGEMENTS

The authors are grateful to Dr. Bastrakov (Geoscience Australia), who performed PRONSPREP97 calculations and provided values for initial guesses of the HKF EoS parameters for  $\text{UO}_2\text{Cl}^+$ ,  $\text{UO}_2\text{Cl}_2$ ,  $\text{UO}_2\text{SO}_4$ , and  $\text{UO}_2(\text{SO}_4)_2^{2-}$ .

## 2.4 APPENDIX 1. $\text{UO}_2^{2+}/\text{Cl}^-$ CHEMICAL SYSTEM

The data considered here are taken from the publications of Ahrland (1951), Davies and Monk (1956), Awasthi and Sundaresan (1981), Choppin and Du (1992), Soderholm et al. (2011), and Migdisov et al. (2018a). The data of Dargent et al. (2014) are not included as we consider the values reported in this manuscript to be erroneous (see Migdisov et al., 2018c)

Table 2.1. Formation constants ( $pK$ ) experimentally derived for  $\text{UO}_2\text{Cl}^+$  ( $\text{UO}_2^{2+} + \text{Cl}^- = \text{UO}_2\text{Cl}^+$ ) together with the derived parameters for the Modified Ryzhenko-Bryzgalin interpolative EoS, the optimized/interpolated values of formation  $pK$ , and errors characterizing quality of the fit.

<b>Complex:</b>		<b><math>\text{UO}_2\text{Cl}^+</math></b>				
<b>Coef.</b>		<b>Basic species</b>				
1		$\text{UO}_2^{2+}$				
1		$\text{Cl}^-$				
<b>Parameter</b>		<b>Reference</b>	<b>init.</b>	<b>opt.</b>	<b><math>\pm</math></b>	
<b><math>pK(298)</math>:</b>	-0.930	Arbitrarily taken	-0.930	0.219	0.048	
<b><math>A(\text{zz}/a)</math>:</b>	0.602	starting parameters	0.602	1.430	0.449	
<b><math>B(\text{zz}/a)</math>:</b>	0.00		0.00	-392.95	214.55	
<b>error:</b>			1.091	0.081		
<b>Experimental point</b>				<b><math>pK</math></b>		
<b><math>T, C</math></b>	<b><math>P, \text{bar}</math></b>	<b>weight</b>	<b>experimental</b>	<b>optimized</b>	<b>error</b>	<b>Data Source</b>
25	sat	2	0.16	0.219	0.059	Soderholm et al. (2011)
25	sat	2	0.17	0.219	0.049	Choppin and Du (1992)
25	sat	2	0.38	0.219	-0.161	Ahrland (1951)
25	sat	2	0.21	0.219	0.009	Davies and Monk (1957)
25	sat	2	0.23	0.219	-0.011	Awasthi and Sundaresan (1980)
25	sat	1	0.02	0.219	0.199	Migdisov et al. (2018)
50	sat	1	0.25	0.279	0.029	Migdisov et al. (2018)
100	sat	1	0.55	0.579	0.029	Migdisov et al. (2018)
150	sat	1	1.09	1.036	-0.054	Migdisov et al. (2018)
200	sat	1	1.59	1.604	0.014	Migdisov et al. (2018)
250	sat	1	2.28	2.286	0.006	Migdisov et al. (2018)



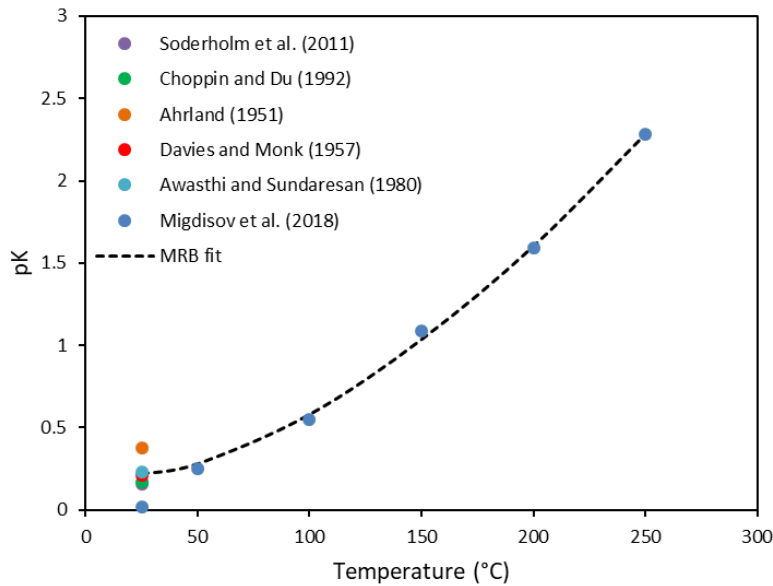


Figure 2.1. The quality of the MRB interpolation performed for the  $UO_2Cl^+$  formation constants ( $pK$ ).

Table 2.2. Formation constants ( $pK$ ) experimentally derived for  $UO_2Cl_2$  ( $UO_2^{2+} + 2Cl^- = UO_2Cl_2$ ) together with the derived parameters for the Modified Ryzhenko-Bryzgalin interpolative EoS, the interpolated values of formation  $pK$ , and errors characterizing quality of the fit.

<b>Complex:</b>		<b><math>UO_2Cl_2</math></b>				
<b>Coef.</b>		<b>Basic species</b>				
1		UO2++				
2		Cl-				
<b>Parameter</b>		<b>Reference</b>		<b>init.</b>	<b>opt.</b>	<b>±</b>
<b><math>pK(298)</math>:</b>	-0.930	Arbitrarily taken		-0.930	0.487	0.499
<b><math>A(zz/a)</math>:</b>	0.602	starting parameters		0.602	-1.134	2.085
<b><math>B(zz/a)</math>:</b>	0.00			0.00	14.10	1084.86
<b>error:</b>				2.559	0.512	
<b>Experimental point</b>				<b><math>pK</math></b>		
<b>T, C</b>	<b>P, bar</b>	<b>weight</b>	<b>experimental</b>	<b>optimized</b>	<b>error</b>	<b>Data Source</b>
25	sat	2	0.1	0.487	0.387	Soderholm et al. (2011)
25	sat	2	1.2	0.487	-0.713	Awasthi and Sundaresan (1980)
25	sat	1	-0.4	0.487	0.887	Migdisov et al. (2018)
50	sat	1	-0.58	0.058	0.638	Migdisov et al. (2018)
100	sat	1	-0.74	-0.785	-0.045	Migdisov et al. (2018)
150	sat	1	-1.44	-1.592	-0.152	Migdisov et al. (2018)
200	sat	1	-2.18	-2.392	-0.212	Migdisov et al. (2018)
250	sat	1	-3.42	-3.246	0.174	Migdisov et al. (2018)

300	sat	1	-4.29	-4.277	0.013	Timofeev et al. (2018)
-----	-----	---	-------	--------	-------	------------------------

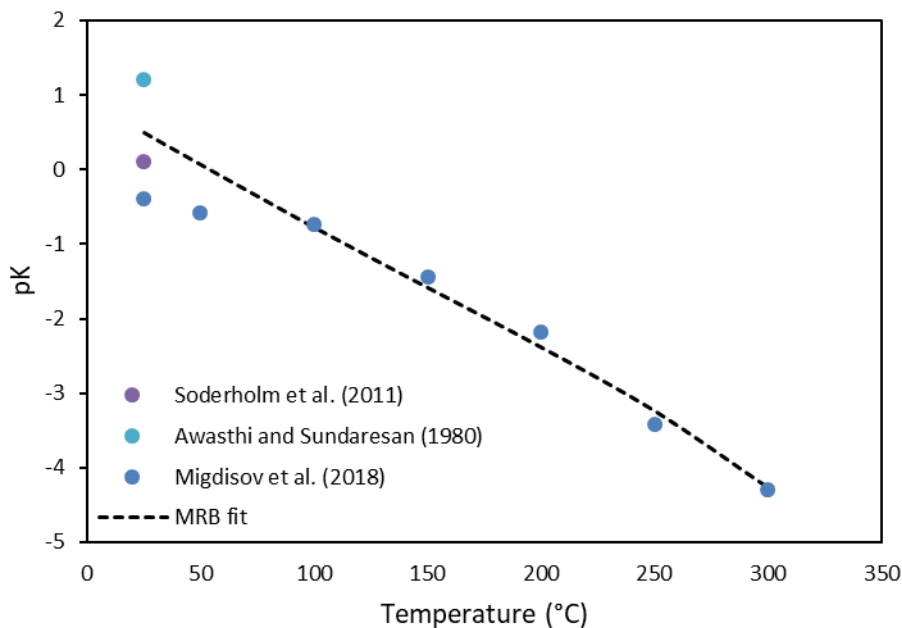


Figure 2.2. The quality of the MRB interpolation performed for the  $UO_2Cl_2$  formation constants (pK).

Table 2.3. Summarized MRB parameters derived for  $UO_2Cl^+$  and  $UO_2Cl_2$ .

	pK (298)	A(zz/a)	B(zz/a)
$UO_2Cl^+$	$0.219 \pm 0.219$	$1.430 \pm 0.449$	$-392.95 \pm 214.55$
$UO_2Cl_2$	$0.487 \pm 0.499$	$-1.134 \pm 2.085$	$14.10 \pm 1084.86$

Table 2.4. Initial estimates of HKF parameters for  $UO_2^{2+}/Cl^-$  species derived using PRONSPREP97 (cal).

Species	$\Delta G^\circ_f$	$\Delta H^\circ_f$	$S^\circ$	$C_p^\circ$	$V^\circ$	$a_1 \times 10$	$a_2 \times 10^{-2}$	$a_3$	$a_4 \times 10^{-4}$	$c_1$	$c_2 \times 10^{-4}$	$c_3 \times 10^{-5}$
$UO_2Cl^+$	-259100	-282614	-6.89	58.81	33.12	6.5185	8.1378	2.5445	-3.1150	45.5015	8.5375	0.6557
$UO_2Cl_2$	-290711	-324681	0.29	107.6	63.63	10.4597	17.7612	-1.2379	-3.5132	68.8767	18.8836	-0.0380

Table 2.5. The HKF optimization performed for  $UO_2Cl^+$  based on the tabulated apparent Gibbs free energies, derived using the interpolation detailed in Table 2.1. The table lists the errors characterizing the fit quality and identify additional constraints used for the fitting. The Optim B code uses and returns HKF parameters in the traditional form: expressed in calories. However, the experimental data included in this table are expressed in kJ.

<b>Species:</b>	<b><math>UO_2Cl^+</math></b>	<b>Reference</b>	<b>correlation a2 -- a4</b>			
<b>Cp(298):</b>	58.810	PRONSPREP97	<b>Cp(298):</b>	58.810	used	
<b>V(298):</b>	33.120	PRONSPREP97	<b>V(298):</b>	33.049		
<b>H(298):</b>	-282614	PRONSPREP97	<b>init.</b>	<b>opt.</b>	<b>stat.</b>	
<b>G(298):</b>	-259100	PRONSPREP97	-259100	-259363	optimized	
<b>S(298):</b>	-6.890	PRONSPREP97	-6.890	-8.773	optimized	
<b>a1*E1:</b>	6.5185	PRONSPREP97	6.5185	6.5185		
<b>a2*E-2:</b>	8.1378	PRONSPREP97	8.1378	8.1378		
<b>a3:</b>	2.5445	PRONSPREP97	2.5445	2.5445		
<b>a4*E-4:</b>	-3.1150	PRONSPREP97	-3.1150	-3.1150		
<b>c1:</b>	45.5015	PRONSPREP97	45.5015	42.4338	optimized	
<b>c2*E-4:</b>	8.5375	PRONSPREP97	8.5375	11.1600	optimized	
<b>w*E-5:</b>	0.6557	PRONSPREP97	0.6840	0.6840		
<b>z:</b>	1		<b>error:</b>	0.695	0.009	
			<b>correlation w=f(S)</b>	0.684058756	used	
<b>G unit:</b>	kJ/mol					
<b>Experimental point</b>			<b>Gibbs free energy</b>			
<b>T, C</b>	<b>P, bar</b>	<b>weight</b>	<b>experimental</b>	<b>initial</b>	<b>optimized</b>	<b>error</b>
25	sat	2	-1085.153	-1084.074	-1085.173	-0.020
30	sat	2	-1084.997	-1083.940	-1085.000	-0.003
50	sat	2	-1084.509	-1083.581	-1084.488	0.021
70	sat	2	-1084.240	-1083.472	-1084.227	0.013
90	sat	2	-1084.179	-1083.579	-1084.176	0.003
110	sat	2	-1084.304	-1083.875	-1084.306	-0.002
130	sat	2	-1084.590	-1084.337	-1084.594	-0.004
150	sat	2	-1085.016	-1084.947	-1085.020	-0.004
170	sat	2	-1085.562	-1085.686	-1085.567	-0.005
190	sat	2	-1086.214	-1086.540	-1086.219	-0.005
210	sat	2	-1086.956	-1087.492	-1086.958	-0.002
230	sat	2	-1087.768	-1088.520	-1087.766	0.001
250	sat	2	-1088.626	-1089.604	-1088.620	0.006

Table 2.6. The HKF optimization performed for  $UO_2Cl_2$  based on the tabulated apparent Gibbs free energies, derived using the interpolation detailed in Table 2.2. The table lists the errors characterizing the fit quality and identify additional constraints used for the fitting. The Optim B code uses and returns HKF parameters in the traditional form: expressed in calories. However, the experimental data included in this table are expressed in kJ.

<b>Species:</b>		<b><math>UO_2Cl_2</math></b>	<b>Reference</b>	<b>correlation a2 -- a4</b>		
<b>Cp(298):</b>	107.600		PRONSPREP97	<b>Cp(298):</b>	107.600	used
<b>V(298):</b>	63.630		PRONSPREP97	<b>V(298):</b>	62.933	
<b>H(298):</b>	-324681		PRONSPREP97	<b>init.</b>	<b>opt.</b>	<b>stat.</b>
<b>G(298):</b>	-290711		PRONSPREP97	-290711	-290703	optimized
<b>S(298):</b>	0.290		PRONSPREP97	0.290	6.026	optimized
<b>a1*E1:</b>	10.4597		PRONSPREP97	10.4597	10.4597	
<b>a2*E-2:</b>	17.7612		PRONSPREP97	17.7612	17.7612	
<b>a3:</b>	-1.2379		PRONSPREP97	-1.2379	-1.2379	
<b>a4*E-4:</b>	-3.5132		PRONSPREP97	-3.5132	-3.5132	
<b>c1:</b>	68.8767		PRONSPREP97	68.8767	2.0543	optimized
<b>c2*E-4:</b>	18.8836		PRONSPREP97	18.8836	53.0537	optimized
<b>w*E-5:</b>	-0.0380		PRONSPREP97	0.2458	0.2458	
<b>z:</b>	0			<b>error:</b>	2.521	0.051
			<b>correlation w=f(S)</b>		0.248743693	used
<b>G unit:</b>	kJ/mol					
<b>Experimental point</b>			<b>Gibbs free energy</b>			
<b>T, C</b>	<b>P, bar</b>	<b>weight</b>	<b>experimental</b>	<b>initial</b>	<b>optimized</b>	<b>error</b>
25	sat	2	-1216.203	-1216.335	-1216.300	-0.097
30	sat	2	-1216.423	-1216.359	-1216.444	-0.021
50	sat	2	-1217.404	-1216.783	-1217.304	0.100
70	sat	2	-1218.556	-1217.662	-1218.474	0.082
90	sat	2	-1219.867	-1218.934	-1219.839	0.028
110	sat	2	-1221.314	-1220.554	-1221.331	-0.017
130	sat	2	-1222.866	-1222.487	-1222.907	-0.041
150	sat	2	-1224.496	-1224.709	-1224.541	-0.045
170	sat	2	-1226.178	-1227.194	-1226.209	-0.031
190	sat	2	-1227.888	-1229.919	-1227.893	-0.005
210	sat	2	-1229.599	-1232.862	-1229.576	0.023
230	sat	2	-1231.272	-1235.999	-1231.240	0.032
250	sat	2	-1232.856	-1239.306	-1232.866	-0.010

Table 2.7. Final recommended values for the HKF EoS for  $UO_2Cl^+$  and  $UO_2Cl_2$  (cal).

Species	$\Delta G^\circ_f$	$\Delta H^\circ_f$	$S^\circ$	$C_p^\circ$	$V^\circ$
$UO_2Cl^+$	-259363	-283470	-8.773	58.81	33.049
$UO_2Cl_2$	-290703	-327415	6.026	107.60	62.933

Species	$a_1 \times 10$	$a_2 \times 10^{-2}$	$a_3$	$a_4 \times 10^{-4}$	$c_1$	$c_2 \times 10^{-4}$	$c_3 \times 10^{-5}$	Z
$UO_2Cl^+$	6.5185	8.1378	2.5445	-3.1150	42.4338	11.1600	0.6840	1
$UO_2Cl_2$	10.4597	17.7612	-1.2379	-3.5132	2.0543	53.0537	0.2458	0

Table 2.8. Tabulated formation constants ( $pK = -\log K$ ) for the reaction  $UO_2^{2+} + Cl^- = UO_2Cl^+$  based on the derived HKF parameters (Table 2.7).

Temperature (°C)	Pressure (bar)			
	Saturated	100	500	1000
25	-0.2228	-0.2059	-0.1509	-0.1067
50	-0.2759	-0.2565	-0.1902	-0.1294
75	-0.4025	-0.3812	-0.3067	-0.235
100	-0.5788	-0.5554	-0.4729	-0.3915
125	-0.7921	-0.7664	-0.6745	-0.583
150	-1.036	-1.0075	-0.9035	-0.8001
175	-1.3067	-1.2752	-1.1555	-1.0376
200	-1.6032	-1.5684	-1.428	-1.2921
225	-1.9272	-1.8894	-1.7198	-1.5614
250	-2.2845	-2.2447	-2.0312	-1.8439
275	-2.6841	-2.647	-2.3631	-2.138
300	-3.1366	-3.1176	-2.7185	-2.4423
325	-3.6589	gas	-3.1047	-2.7559
350	-4.313	gas	-3.5486	-3.0785

Table 2.9. Tabulated formation constants ( $pK = -\log K$ ) for the reaction  $UO_2^{2+} + 2Cl^- = UO_2Cl_2$  based on the derived HKF parameters (Table 2.7).

Temperature (°C)	Pressure (bar)			
	Saturated	100	500	1000
25	-0.1942	-0.1559	-0.0252	0.094
50	-0.3122	-0.2717	-0.1302	0.0073
75	-0.5406	-0.498	-0.347	-0.1959
100	-0.8264	-0.7808	-0.6182	-0.4537
125	-1.1481	-1.0987	-0.9208	-0.7404
150	-1.4978	-1.4438	-1.245	-1.0445
175	-1.874	-1.8145	-1.5876	-1.3615
200	-2.2783	-2.213	-1.9485	-1.6902
225	-2.7177	-2.6471	-2.3295	-2.0302
250	-3.2059	-3.132	-2.7335	-2.3816
275	-3.7614	-3.6928	-3.165	-2.744
300	-4.4039	-4.3692	-3.6308	-3.1167
325	-5.1604	gas	-4.1455	-3.4992
350	-6.1305	gas	-4.7602	-3.8918

## 2.5 APPENDIX 2. $UO_2^{2+}/SO_4^{2-}$ CHEMICAL SYSTEM

The data considered here are taken from the publications of Geipel et al. (1996), Guillaumont et al. (2003), Vercouter et al. (2008), Tian and Rao (2009), Vopálka et al. (2010), Berto et al. (2012), Alcorn et al. (2019), and Kalintsev et al. (2019).

Table 2.10. Formation constants ( $pK$ ) experimentally derived for  $UO_2SO_4$  ( $UO_2^{2+} + SO_4^{2-} = UO_2SO_4$ ) together with the derived parameters for the Modified Ryzhenko-Bryzgalin interpolative EoS, the optimized/interpolated values of formation  $pK$ , and errors characterizing quality of the fit.

<b>Complex:</b>		<b><math>UO_2SO_4</math></b>				
<b>Coef.</b>		<b>Basic species</b>				
1		UO2++				
1		SO4--				
<b>Parameter</b>		<b>Reference</b>	<b>init.</b>	<b>opt.</b>	<b>±</b>	
<b>pK(298):</b>	-3.150	Arbitrarily taken	3.150	3.286	0.125	
<b>A(zz/a):</b>	1.602	starting parameters	1.602	2.177	0.191	
<b>B(zz/a):</b>	0.00		0.00	-205.57	106.89	
<b>error:</b>			0.568	0.234		
<b>Experimental point</b>				<b>pK</b>		
<b>T, C</b>	<b>P, bar</b>	<b>weight</b>	<b>experimental</b>	<b>optimized</b>	<b>error</b>	<b>Data Source</b>
25	sat	1	3.15	3.286	0.136	Guillaumont et al. (2003)
25	sat	1	3.03	3.286	0.256	Vopalka et al. (2010)
25	sat	1	3.23	3.286	0.056	Tian and Rao (2009)
25	sat	1	3.29	3.286	-0.004	Vercouter et al. (2008)
25	sat	1	3.4	3.286	-0.114	Berto et al. (2012)
25	sat	1	3.35	3.286	-0.064	Geipel et al. (1996)
25	sat	2	3.3	3.286	-0.014	Kalintsev et al. (2019)
25	sat	1	3.67	3.286	-0.384	Alcorn et al. (2019)
25	sat	1	3.03	3.286	0.256	Alcorn et al. (2019)
25	sat	1	3.11	3.286	0.176	Alcorn et al. (2019)
25	sat	1	3.23	3.286	0.056	Alcorn et al. (2019)
70	sat	1	3.74	3.876	0.136	Tian and Rao (2009)
70	sat	1	4.18	3.876	-0.304	Vercouter et al. (2008)
75	sat	1	4.31	3.954	-0.356	Alcorn et al. (2019)
75	sat	1	3.91	3.954	0.044	Alcorn et al. (2019)
75	sat	1	3.98	3.954	-0.026	Alcorn et al. (2019)
75	sat	1	3.77	3.954	0.184	Alcorn et al. (2019)
100	sat	3	4.4	4.367	-0.033	Kalintsev et al. (2019)

125	sat	1	4.83	4.813	-0.017	Alcorn et al. (2019)
125	sat	1	4.58	4.813	0.233	Alcorn et al. (2019)
125	sat	1	4.61	4.813	0.203	Alcorn et al. (2019)
150	sat	3	5.44	5.287	-0.153	Kalintsev et al. (2019)
175	sat	1	5.65	5.791	0.141	Alcorn et al. (2019)
175	sat	1	5.45	5.791	0.341	Alcorn et al. (2019)
175	sat	1	5.47	5.791	0.321	Alcorn et al. (2019)
200	sat	3	6.33	6.328	-0.002	Kalintsev et al. (2019)
225	sat	1	6.6	6.909	0.309	Alcorn et al. (2019)
225	sat	1	6.56	6.909	0.349	Alcorn et al. (2019)
225	sat	1	6.53	6.909	0.379	Alcorn et al. (2019)
250	sat	3	7.74	7.55	-0.19	Kalintsev et al. (2019)
275	sat	1	7.86	8.276	0.416	Alcorn et al. (2019)
275	sat	1	7.89	8.276	0.386	Alcorn et al. (2019)
275	sat	1	7.82	8.276	0.456	Alcorn et al. (2019)
325	sat	1	10.07	10.217	0.147	Alcorn et al. (2019)
325	sat	1	9.77	10.217	0.447	Alcorn et al. (2019)
325	sat	1	9.54	10.217	0.677	Alcorn et al. (2019)
350	sat	1	12.35	11.806	-0.544	Alcorn et al. (2019)
350	sat	1	12.62	11.806	-0.814	Alcorn et al. (2019)
350	sat	1	11.75	11.806	0.056	Alcorn et al. (2019)

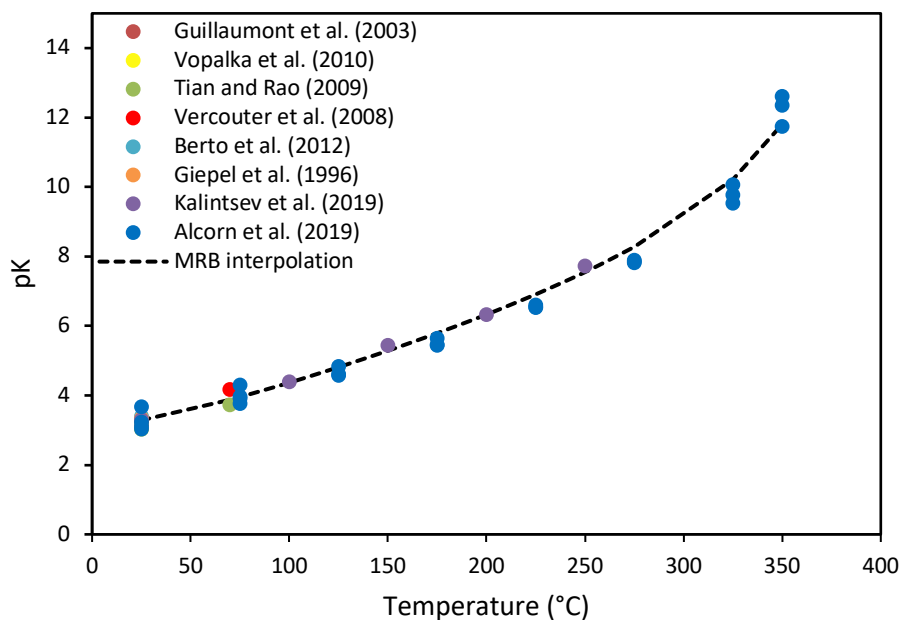


Figure 2.3. The quality of the MRB interpolation performed for the  $UO_2SO_4$  formation constants (pK).



Table 2.11. Formation constants (*pK*) experimentally derived for  $UO_2(SO_4)_2^{2-}$  ( $UO_2^{2+} + 2 SO_4^{2-} = UO_2(SO_4)_2^{2-}$ ) together with the derived parameters for the Modified Ryzhenko-Bryzgalin interpolative EoS, the optimized/interpolated values of formation *pK*, and errors characterizing quality of the fit.

<b>Complex:</b>		<b><math>UO_2(SO_4)_2^{2-}</math></b>				
<b>Coef.</b>		<b>Basic species</b>				
1		UO2++				
2		SO4--				
<b>Parameter</b>		<b>Reference</b>		<b>init.</b>	<b>opt.</b>	<b>±</b>
<b>pK(298):</b>	3.150	Arbitrarily taken		3.150	4.311	0.076
<b>A(zz/a):</b>	1.602	starting parameters		1.602	2.502	0.278
<b>B(zz/a):</b>	0.00			0.00	-117.80	140.10
<b>error:</b>				1.679	0.291	
<b>Experimental point</b>				<b>pK</b>		
<b>T, C</b>	<b>P, bar</b>	<b>weight</b>	<b>experimental</b>	<b>optimized</b>	<b>error</b>	<b>Data Source</b>
25	sat	3	4.1	4.311	0.211	Kalintsev et al. (2019)
25	sat	3	4.14	4.311	0.171	Guillaumont et al. (2003)
25	sat	3	3.95	4.311	0.361	Vopalka et al. (2010)
25	sat	3	4.22	4.311	0.091	Tian and Rao (2009)
25	sat	3	4.33	4.311	-0.019	Vercouter et al. (2008)
25	sat	3	4.62	4.311	-0.309	Berto et al. (2012)
25	sat	3	4.21	4.311	0.101	Giepel et al. (1996)
25	sat	3	4.62	4.311	-0.309	Alcorn et al. (2019)
70	sat	3	5.34	5.142	-0.198	Tian and Rao (2009)
70	sat	3	5.57	5.142	-0.428	Vercouter et al. (2008)
75	sat	2	5.9	5.246	-0.654	Alcorn et al. (2019)
100	sat	3	5.26	5.786	0.526	Kalintsev et al. (2019)
125	sat	1	6.73	6.354	-0.376	Alcorn et al. (2019)
150	sat	3	6.83	6.946	0.116	Kalintsev et al. (2019)
175	sat	1	8.04	7.566	-0.474	Alcorn et al. (2019)
200	sat	3	8	8.223	0.223	Kalintsev et al. (2019)
225	sat	1	9.53	8.928	-0.602	Alcorn et al. (2019)
250	sat	3	9.7	9.704	0.004	Kalintsev et al. (2019)
275	sat	1	11.05	10.582	-0.468	Alcorn et al. (2019)
325	sat	1	13.15	12.938	-0.212	Alcorn et al. (2019)
350	sat	1	14.97	14.88	-0.09	Alcorn et al. (2019)

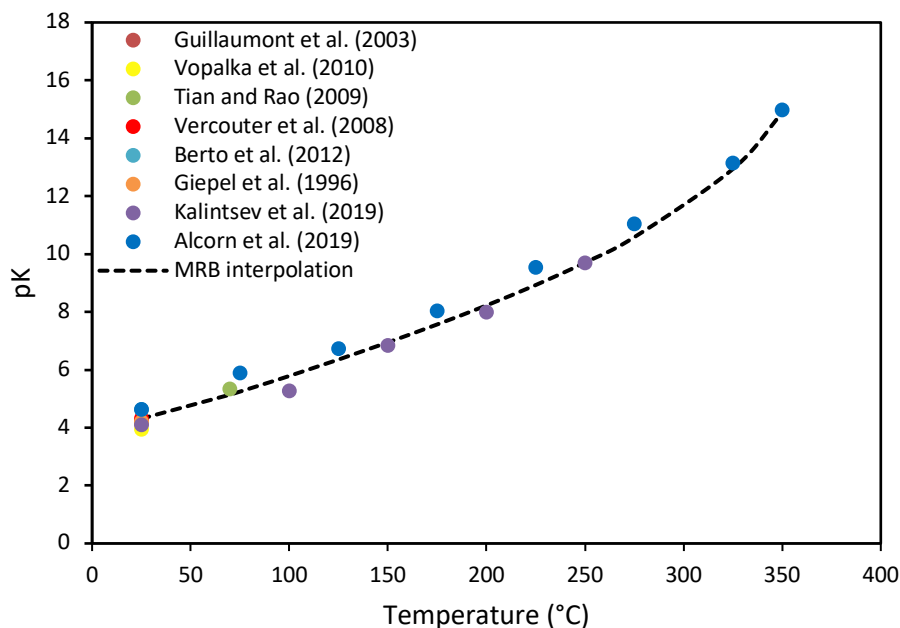


Figure 2.4. The quality of the MRB interpolation performed for the  $UO_2(SO_4)_2^{2-}$  formation constants (pK).

Table 2.12. Summarized MRB parameters derived for  $UO_2SO_4$  and  $UO_2(SO_4)_2^{2-}$ .

	pK (298)	A(zz/a)	B(zz/a)
$UO_2SO_4$	$3.286 \pm 0.125$	$2.177 \pm 0.191$	$-205.57 \pm 106.89$
$UO_2(SO_4)_2^{2-}$	$4.311 \pm 0.076$	$2.502 \pm 0.278$	$-117.8 \pm 140.10$

Table 2.13. Initial estimates of HKF parameters for  $UO_2^{2+}/SO_4^{2-}$  species derived using PRONSPREP97 (cal).

Species	$\Delta G^\circ_f$	$\Delta H^\circ_f$	$S^\circ$	$C_p^\circ$	$V^\circ$	$a_1 \times 10$	$a_2 \times 10^{-2}$	$a_3$	$a_4 \times 10^{-4}$	$c_1$	$c_2 \times 10^{-4}$	$\omega \times 10^{-5}$
$UO_2SO_4$	-410262	-469461	-31.94	-8.04	29.21	5.749	6.2589	3.283	-3.0377	1.105	-4.6722	-0.038
$UO_2(SO_4)_2^{2-}$	-589665	-702115	-73.66	-47.25	55.37	10.8057	18.606	-1.5699	-3.5481	18.3904	-12.6602	4.3328

Table 2.14. The HKF optimization performed for  $UO_2(SO_4)$  based on the tabulated apparent Gibbs free energies, derived using the interpolation detailed in Table 2.2. The table lists the errors characterizing the fit quality and identify additional constraints used for the fitting. The Optim B code uses and returns HKF parameters in the traditional form: expressed in calories. However, the experimental data included in this table are expressed in kJ.

<b>Species:</b> $UO_2SO_4$		<b>Reference</b>	<b>correlation a2 -- a4</b>			
<b>Cp(298):</b>	-8.040	PRONSPREP97	<b>Cp(298):</b>	-8.040	used	
<b>V(298):</b>	29.210	PRONSPREP97	<b>V(298):</b>	28.577		
<b>H(298):</b>	-469461	PRONSPREP97	<b>init.</b>	<b>opt.</b>	<b>stat.</b>	
<b>G(298):</b>	-410262	PRONSPREP97	-410262	-410271	optimized	
<b>S(298):</b>	-31.940	PRONSPREP97	-31.940	8.087	optimized	
<b>a1*E1:</b>	5.7490	PRONSPREP97	5.7490	5.7490		
<b>a2*E-2:</b>	6.2589	PRONSPREP97	6.2589	6.2589		
<b>a3:</b>	3.2830	PRONSPREP97	3.2830	3.2830		
<b>a4*E-4:</b>	-3.0377	PRONSPREP97	-3.0377	-3.0377		
<b>c1:</b>	1.1050	PRONSPREP97	1.1050	87.9933	optimized	
<b>c2*E-4:</b>	-4.6722	PRONSPREP97	-4.6722	-46.2721	optimized	
<b>w*E-5:</b>	-0.0380	PRONSPREP97	0.2175	0.2175		
<b>z:</b>	0		<b>error:</b>	47.626	1.181	
<b>G unit:</b>	kJ/mol		<b>correlation w=f(S)</b>		0.217524827	used
<b>Experimental point</b>			<b>Gibbs free energy</b>			
<b>T, C</b>	<b>P, bar</b>	<b>weight</b>	<b>experimental</b>	<b>initial</b>	<b>optimized</b>	<b>error</b>
25	sat	1	-1715.828	-1716.536	-1716.576	-0.748
50	sat	1	-1717.056	-1713.158	-1717.462	-0.406
75	sat	1	-1718.678	-1709.728	-1718.611	0.067
100	sat	1	-1720.645	-1706.262	-1720.155	0.490
125	sat	1	-1722.900	-1702.761	-1722.133	0.767
150	sat	1	-1725.406	-1699.229	-1724.554	0.852
175	sat	1	-1728.136	-1695.661	-1727.408	0.728
200	sat	1	-1731.087	-1692.049	-1730.676	0.411
225	sat	1	-1734.252	-1688.382	-1734.330	-0.078
250	sat	1	-1737.622	-1684.640	-1738.335	-0.713
275	sat	1	-1741.236	-1680.794	-1742.646	-1.410
300	sat	1	-1745.340	-1676.787	-1747.193	-1.853
325	sat	1	-1750.693	-1672.505	-1751.844	-1.151
350	sat	1	-1759.281	-1667.597	-1756.237	3.044

Table 2.15. The HKF optimization performed for  $UO_2(SO_4)_2$  based on the tabulated apparent Gibbs free energies, derived using the interpolation detailed in Table 2.2. The table lists the errors characterizing the fit quality and identify additional constraints used for the fitting. The Optim B code uses and returns HKF parameters in the traditional form: expressed in calories. However, the experimental data included in this table are expressed in kJ.

<b>Species:</b>	<b><math>UO_2(SO_4)^{2-}</math></b>	<b>Reference</b>	<b>correlation a2 -- a4</b>			
<b>Cp(298):</b>	-47.250	PRONSPREP97	<b>Cp(298):</b>	-47.250	used	
<b>V(298):</b>	55.370	PRONSPREP97	<b>V(298):</b>	58.892		
<b>H(298):</b>	-702115	PRONSPREP97	<b>init.</b>	<b>opt.</b>	<b>stat.</b>	
<b>G(298):</b>	-589665	PRONSPREP97	-589665	-589732	optimized	
<b>S(298):</b>	-73.660	PRONSPREP97	-73.660	20.215	optimized	
<b>a1*E1:</b>	10.8057	PRONSPREP97	10.8057	10.8057	optimized	
<b>a2*E-2:</b>	18.6060	PRONSPREP97	18.6060	18.6060		
<b>a3:</b>	-1.5699	PRONSPREP97	-1.5699	-1.5699		
<b>a4*E-4:</b>	-3.5481	PRONSPREP97	-3.5481	-3.5481		
<b>c1:</b>	18.3904	PRONSPREP97	18.3904	113.0653		
<b>c2*E-4:</b>	-12.6602	PRONSPREP97	-12.6602	-65.7177		
<b>w*E-5:</b>	4.3328	PRONSPREP97	2.9058	2.9058		
<b>z:</b>	-2					
		<b>error:</b>	90.730	1.670		
		<b>correlation w=f(S)</b>		2.905858694		used
<b>G unit:</b> kJ/mol						
<b>Experimental point</b>			<b>Gibbs free energy</b>			
<b>T, C</b>	<b>P, bar</b>	<b>weight</b>	<b>experimental</b>	<b>initial</b>	<b>optimized</b>	<b>error</b>
25	sat	1	-2466.138	-2467.158	-2467.441	-1.303
50	sat	1	-2468.917	-2459.328	-2469.459	-0.542
75	sat	1	-2471.790	-2451.289	-2471.541	0.249
100	sat	1	-2474.728	-2443.063	-2473.862	0.866
125	sat	1	-2477.670	-2434.626	-2476.458	1.212
150	sat	1	-2480.563	-2425.944	-2479.308	1.255
175	sat	1	-2483.351	-2416.964	-2482.359	0.993
200	sat	1	-2485.990	-2407.611	-2485.524	0.466
225	sat	1	-2488.404	-2397.771	-2488.678	-0.274
250	sat	1	-2490.466	-2387.270	-2491.629	-1.163
275	sat	1	-2492.043	-2375.844	-2494.097	-2.054
300	sat	1	-2493.155	-2363.099	-2495.674	-2.519
325	sat	1	-2494.191	-2348.307	-2495.616	-1.425
350	sat	1	-2495.918	-2329.238	-2491.678	4.240

Table 2.16. Final recommended values for the HKF EoS for  $UO_2SO_4$  and  $UO_2(SO_4)_2^{2-}$  (cal).

Species	$\Delta G^\circ_f$	$\Delta H^\circ_f$	$S^\circ$	$C_p^\circ$	$V^\circ$
$UO_2SO_4$	-410271	-457570	8.087	-8.040	28.577
$UO_2(SO_4)_2^{2-}$	-589732	-674239	20.215	-47.250	58.892

Species	$a_1 \times 10$	$a_2 \times 10^{-2}$	$a_3$	$a_4 \times 10^{-4}$	$c_1$	$c_2 \times 10^{-4}$	$\omega \times 10^{-5}$	Z
$UO_2SO_4$	5.7490	6.2589	3.2830	-3.0377	87.9933	-46.2721	0.2175	0
$UO_2(SO_4)_2^{2-}$	10.8057	18.6060	-1.5699	-3.5481	113.0653	-65.7177	2.9058	-2

Table 2.17. Tabulated formation constants ( $pK = -\log K$ ) for the reaction  $UO_2^{++} + SO_4^{2-} = UO_2SO_4$  based on the derived HKF parameters (Table 2.16).

Temperature (°C)	Pressure (bar)			
	Saturated	100	500	1000
25	-3.4166	-3.3999	-3.3538	-3.3352
50	-3.6504	-3.6329	-3.5822	-3.555
75	-3.9431	-3.9233	-3.8629	-3.8231
100	-4.298	-4.2742	-4.1995	-4.1436
125	-4.7118	-4.6829	-4.5887	-4.5127
150	-5.1816	-5.1463	-5.0264	-4.9251
175	-5.7053	-5.6623	-5.5091	-5.3766
200	-6.2822	-6.231	-6.0345	-5.8635
225	-6.9169	-6.8573	-6.6013	-6.3829
250	-7.6205	-7.5541	-7.2095	-6.9318
275	-8.4095	-8.3448	-7.8606	-7.5066
300	-9.301	-9.2672	-8.5592	-8.1039
325	-10.3174	gas	-9.3177	-8.7206
350	-11.5502	gas	-10.1884	-9.3549

Table 2.18. Tabulated formation constants ( $pK = -\log K$ ) for the reaction  $UO_2^{++} + 2SO_4^{2-} = UO_2(SO_4)_2^{2-}$  based on the derived HKF parameters (Table 2.16).

Temperature (°C)	Pressure (bar)			
	Saturated	100	500	1000
25	-4.5388	-4.4943	-4.353	-4.2462
50	-4.8322	-4.7912	-4.6606	-4.5608
75	-5.2081	-5.1673	-5.036	-4.9328
100	-5.6642	-5.6212	-5.4813	-5.3675
125	-6.1932	-6.1463	-5.9904	-5.8598
150	-6.7895	-6.737	-6.5571	-6.4028
175	-7.4487	-7.3893	-7.1762	-6.9907
200	-8.1691	-8.1022	-7.8442	-7.619
225	-8.9547	-8.8802	-8.5588	-8.2837
250	-9.8172	-9.7372	-9.3198	-8.9809
275	-10.7747	-10.6988	-10.1284	-9.7067
300	-11.8466	-11.8075	-10.9898	-10.4569
325	-13.0594	gas	-11.9177	-11.2284
350	-14.521	gas	-12.9701	-12.019

### 3. REFERENCES

- Ahrland S. (1951) On the Complex Chem of the Uranyl Ion. VI. The complexity of uranyl chloride, bromide and nitrate. *Acta Chem. Scand.* **5**, 1271–1282.
- Alcorn C. D., Cox J. S., Applegarth L. M. S. G. A. and Tremaine P. R. (2019) Investigation of Uranyl Sulfate Complexation under Hydrothermal Conditions by Quantitative Raman Spectroscopy and Density Functional Theory. *J. Phys. Chem. B* **123**, 7385–7409.
- Awasthi S. P. and Sundaresan M. (1981) Spectrophotometric & calorimetric study of uranyl cation/chloride anion system in aqueous solution. *Indian J. Chem.* **20A**, 378–381.
- Bailey E. H. and Vala Ragnarsdottir K. (1994) Uranium and thorium solubilities in subduction zone fluids. *Earth Planet. Sci. Lett.* **124**, 119–129.
- Bastrakov E., Jaireth S. and Mernagh T. (2010) Vol. Record 2010/29. *ed Geosci. Aust.* **91**.
- Berto S., Crea F., Daniele P. G., Gianguzza A., Pettignano A. and Sammartano S. (2012) Advances in the investigation of dioxouranium(VI) complexes of interest for natural fluids. *Coord. Chem. Rev.* **256**, 63–81.
- Blanco Martín L., Rutqvist J. and Birkholzer J. T. (2015) Long-term modeling of the thermal-hydraulic-mechanical response of a generic salt repository for heat-generating nuclear waste. *Eng. Geol.* **193**, 198–211.
- Born M. (1920) Volumen und Hydrationswärme der Ionen. *Ziet. Phys.* **1**, 45–48.
- Bruno J. and Ewing R. C. (2006) Spent nuclear fuel. *Elements* **2**, 343–349.
- Buscheck T. A., Glascoe L. G., Lee K. H., Gansemer J., Sun Y. and Mansoor K. (2003) Validation of the Multiscale Thermohydrologic Model used for analysis of a proposed repository at Yucca Mountain. *J. Contam. Hydrol.* **62–63**, 421–440.
- Choppin G. R. and Du M. (1992) *f*-Element Complexation in Brine Solutions. *Radiochim. Acta* **58/59**, 101–104.
- Chou I.-M., Burruss R. C. and Lu W. (2005) Advances in High-Pressure Technology for Geophysical Applications. In *Advances in High-Pressure technology for Geophysical Applications* pp. 475–485.
- Clark D. L., Hobart D. E. and Neu M. P. (1995) Actinide Carbonate Complexes and Their Importance in Actinide Environmental Chemistry. *Chem. Rev.* **95**, 25–48.

- Cuney M. (1978) Geologic environment, mineralogy, and fluid inclusions of the Bois Noirs-Limouzat uranium vein, Forez, France. *Econ. Geol.* **73**, 1567–1610.
- Dargent M., Dubessy J., Truche L., Bazarkina E. F., Nguyen-Trung C. and Robert P. (2014) Experimental study of uranyl(VI) chloride complex formation in acidic LiCl aqueous solutions under hydrothermal conditions ( $T = 21\text{--}350\text{ }^{\circ}\text{C}$ , Psat) using Raman spectroscopy. *Eur. J. Mineral.* **25**, 765–775.
- Davies E. W. and Monk C. B. (1956) Spectrophotometric studies of electrolytic dissociation. *Trans. Faraday Soc.* **53**, 442–449.
- Dhakal D., Akram N., Mayanovic R. A., Boukhalifa H. and Xu H. (2020) A Study of Uranyl (VI) Chloride Complexes in Aqueous Solutions under Hydrothermal Conditions using Raman Spectroscopy. *MRS Adv.*, 2623–2629.
- Dhakal D., Mayanovic R. A., Baker J. L., Boukhalifa H., Xu H. and Sun C. J. (2019) Design of a containment apparatus for synchrotron XAS measurements of radioactive fluid samples under high temperatures and pressures. *Rev. Sci. Instrum.* **90**.
- Duan Z. and Sun R. (2003) An improved model calculating CO<sub>2</sub> solubility in pure water and aqueous NaCl solutions from 273 to 533 K and from 0 to 2000 bar. *Chem. Geol.* **193**, 257–271.
- Ewing R. C. (2015) Long-term storage of spent nuclear fuel. *Nat. Mater.* **14**, 252–257.
- Geipel G., Brachmann A., Brendler V., Bernhard G. and Nitsche H. (1996) Uranium(VI) Sulfate Complexation Studied by Time-Resolved Laser-Induced Fluorescence Spectroscopy (TRLFS). *Radiochim. Acta* **75**, 199–204.
- Götz C., Geipel G. and Bernhard G. (2011) The influence of the temperature on the carbonate complexation of uranium(VI): A spectroscopic study. *J. Radioanal. Nucl. Chem.* **287**, 961–969.
- Greenberg H., Wen J. and Buscheck T. A. (2013) *Scoping Thermal Analysis of Alternative Dual-Purpose Canister Disposal Concepts.*
- Greenburg H. R. and Wen J. (2013) *Repository layout and host rock thermal gradient trade study for large waste packages in clay/shale: Using the DSEF thermal analytical model.*
- Guillaumont R., Fanghänel T., Fuger J., Grenthe I., Neck V., Palmer D. A. and Rand M. H. (2003) *Update on the chemical thermodynamics of uranium, neptunium, plutonium, americium and technetium.*
- Guo X., Wu D., Ushakov S., Shvareva T., Xu H. and Navrotsky A. (2019) Energetics of hydration on



- uranium oxide and peroxide surfaces. *J. Mater. Res.*
- Hardin E. L., Clayton D. J., Howard R. L., Scaglione J. M., Pierce E., Banerjee K., Voegelé M. D., Greenberg H. R., Wen J., Buscheck T. A., Carter J. T., Severynse T. and Nutt W. M. (2013) *Preliminary Report on Dual-Purpose Canister Disposal Alternatives (FY13)*.,
- Hardin E., Price L., Kalinina E. A., Hadgu T., Ilgen A. G., Bryan C. R., Scaglione J. M., Banerjee K., Clarity J., Jubin R., Sobes V., Howard R., Carter J., Sverynse T. and Perry F. (2015) *Summary of Investigations on Technical Feasibility of Direct Disposal of Canisters*.,
- Haukwa C. B., Wu Y. S. and Bodvarsson G. S. (2003) Modeling thermal-hydrological response of the unsaturated zone at Yucca Mountain, Nevada, to thermal load at a potential repository. *J. Contam. Hydrol.* **62–63**, 529–552.
- Helgeson H. C., Kirkham D. H. and Flowers G. C. (1981) Theoretical prediction of the thermodynamic behavior of aqueous electrolytes at high pressures and temperatures: IV. Calculation of activity coefficients, osmotic coefficients, and apparent molal and standard and relative partial molal properties to 600°C. *Am. J. Sci.* **281**.
- Hem J. D. (1985) U.S Geological Survey Water Supply Paper 2254. *United States Gov. Print. Off.* **2254**.
- Higgins N. C. (1980) Fluid Inclusion Evidence for the Transport of Tungsten By Carbonate Complexes in Hydrothermal Solutions. *Can. J. Earth Sci.* **17**, 823–830.
- Hill R. J. and Howard C. J. (1987) Quantitative phase analysis from neutron powder diffraction data using the Rietveld method. *J. Appl. Crystallogr.* **20**, 467–474.
- Johnson J. W., Oelkers E. H. and Helgeson H. C. (1992) SUPCRT92: A software package for calculating the standard molal thermodynamic properties of minerals, gases, aqueous species, and reactions from 1 to 5000 bar and 0 to 1000 °C. *Comput. Geosci.* **18**, 899–947.
- Johnson L., Niemeyer M., Klubertanz G., Siegel P. and Gribi P. (2002) *Calculations of the temperature evolution of a repository for spent fuel, vitrified high-level waste and intermediate level waste in Opalinus Clay*.,
- Kalintsev A., Migdisov A. A., Alcorn C. D., Baker J. L., Brugger J., Mayanovic R. A., Akram N., Guo X., Xu H., Boukhalfa H., Caporuscio F. A., Viswanathan C., Jove-Colon C., Want Y., Matteo E. and Roback R. Uranium carbonate complexes demonstrate drastic decrease in stability at elevated temperatures. *Commun. Chem.* *\_in\_press*.
- Kalintsev A., Migdisov A., Xu H., Roback R. and Brugger J. (2019) Uranyl speciation in sulfate-bearing

- hydrothermal solutions up to 250 °C. *Geochim. Cosmochim. Acta* **267**, 75–91.
- Kulik D. A., Wagner T., Dmytrieva S. V., Kosakowski G., Hingerl F. F., Chudnenko K. V. and Berner U. R. (2013) GEM-Selektor geochemical modeling package: Revised algorithm and GEMS3K numerical kernel for coupled simulation codes. *Comput. Geosci.* **17**, 1–24.
- Liu W., Migdisov A. and Williams-Jones A. (2012) The stability of aqueous nickel(II) chloride complexes in hydrothermal solutions: Results of UV–Visible spectroscopic experiments. *Geochim. Cosmochim. Acta* **94**, 276–290. Available at: <http://linkinghub.elsevier.com/retrieve/pii/S0016703712002712> [Accessed September 21, 2012].
- Marshall W. L. and Franck E. U. (1981) Ion Product of Water Substance, 0-1000°C, 1-10,000 Bars. New International Formulation and Its Background. *J. Phys. Chem. Ref. Data* **10**, 295–304.
- McLennan S. M. and Taylor S. R. (1979) Rare earth element mobility associated with uranium mineralisation. *Nature* **282**, 247–250.
- Migdisov A. A., Boukhalfa H., Timofeev A., Runde W., Roback R. and Williams-Jones A. E. (2018a) A spectroscopic study of uranyl speciation in chloride-bearing solutions at temperatures up to 250 °C. *Geochim. Cosmochim. Acta* **222**, 130–145.
- Migdisov A. A., Boukhalfa H., Timofeev A., Runde W., Roback R. and Williams-Jones A. E. (2018b) A spectroscopic study of uranyl speciation in chloride-bearing solutions at temperatures up to 250 °C. *Geochim. Cosmochim. Acta* **222**, 130–145.
- Migdisov A. A., Runde W., Williams-Jones A. E., Boukhalfa H., Roback R. and Timofeev A. (2018c) Response to the comment “Uranyl-chloride speciation and uranium transport in hydrothermal brines: Comment on Migdisov et al. (2018)” by Dargent et al. *Geochim. Cosmochim. Acta* **235**, 509–512. Available at: <https://doi.org/10.1016/j.gca.2018.06.015>.
- Miron G. D., Wagner T., Kulik D. A. and Heinrich C. A. (2016) Internally consistent thermodynamic data for aqueous species in the system Na-K-Al-Si-O-H-Cl. *Geochim. Cosmochim. Acta* **187**, 41–78.
- Nisbet H., Migdisov A. A., Williams-jones A. E., Hinsberg V. J. Van, Xu H. and Roback R. (2021) The solubility of thorium in carbonate-bearing solutions at hydrothermal conditions. *Geochim. Cosmochim. Acta*. Available at: <https://doi.org/10.1016/j.gca.2021.04.035>.
- Oelkers E. H. and Helgeson H. C. (1991) Calculation of activity coefficients and degrees of formation of neutral ion pairs in supercritical electrolyte solutions. *Geochim. Cosmochim. Acta* **55**.
- Oelkers E. H. and Helgeson H. C. (1990) Triple-ion anions and polynuclear complexing in supercritical electrolyte solutions. *Geochim. Cosmochim. Acta* **54**, 727–738.

- Ondruš P., Veselovský F., Gabašová A., Drábek M., Dobeš P., Malý K., Hloušek J. and Sejkora J. (2003) Ore-forming processes and mineral parageneses of the Jáchymov ore district. *J. Czech Geol. Soc.* **48**, 157–192.
- Pokrovskii V. and Helgeson H. C. (1997) Calculation of the standard partial molal thermodynamic properties of KClO and activity coefficients of aqueous KCl at temperatures and pressures to 1000 ̡ and 5. *Geochim. Cosmochim. Acta* **61**, 2175–2183. Available at: <http://linkinghub.elsevier.com/retrieve/pii/S0016703797000707> [Accessed July 15, 2010].
- Ravel B. and Newville M. (2005) ATHENA, ARTEMIS, HEPHAESTUS: data analysis for X-ray absorption spectroscopy using IFEFFIT. *J. Synchrotron Radiat.* **12**, 537–541.
- Runde W. (2015) Geochemical interactions of actinides in the environment. *Geochemistry Soil Radionuclides* **103**, 21–44.
- Ryzhenko B. N., Bryzgalin O. V., Artamkina I. Y., Spasennykh M. Y. and Shapkin A. I. (1985) An electrostatic model for the electrolytic dissociation of inorganic substances dissolved in water. *Geochem. Int.* **22**, 138–144.
- Shock E. L. and Helgeson H. C. (1988) Calculation of the thermodynamic and transport properties of aqueous species at high pressures and temperatures: Correlation algorithms for ionic species and equation of state predictions to 5 kb and 1000°C. *Geochim. Cosmochim. Acta* **52**, 2009–2036. Available at: <http://linkinghub.elsevier.com/retrieve/pii/0016703788901810>.
- Shock E. L., Oelkers E. H., Johnson J. W., Sverjensky D. a. and Helgeson H. C. (1992) Calculation of the thermodynamic properties of aqueous species at high pressures and temperatures. Effective electrostatic radii, dissociation constants and standard partial molal properties to 1000 ̡C and 5 kbar. *J. Chem. Soc. Faraday Trans.* **88**, 803. Available at: <http://xlink.rsc.org/?DOI=ft9928800803>.
- Shock E. L., Sassani D. C., Willis M. and Sverjensky D. A. (1997a) Inorganic species in geologic fluids: correlations among standard molal thermodynamic properties of aqueous ions and hydroxide complexes. *Geochim. Cosmochim. Acta* **61**, 907–50. Available at: <http://www.ncbi.nlm.nih.gov/pubmed/11541225>.
- Shock E. L., Sassani D. C., Willis M. and Sverjensky D. A. (1997b) Inorganic species in geologic fluids: correlations among standard molal thermodynamic properties of aqueous ions and hydroxide complexes. *Geochim. Cosmochim. Acta* **61**, 907–950.
- Shvarov Y. (2015) A suite of programs, OptimA, OptimB, OptimC, and OptimS compatible with the

- Unitherm database, for deriving the thermodynamic properties of aqueous species from solubility, potentiometry and spectroscopy measurements. *Appl. Geochemistry* **55**, 17–27.
- Skirrow R. G. (2009) Uranium mineral systems: processes, exploration criteria and a new deposit framework. *Geosci. Aust. Rec.* **20**.
- Soderholm L., Skanthakumar S. and Wilson R. E. (2011) Structural correspondence between uranyl chloride complexes in solution and their stability Constants. *J. Phys. Chem. A* **115**, 4959–4967.
- Staupe S., Werner W., Mordhorst T., Wemmer K., Jacob D. E. and Markl G. (2012) Multi-stage Ag-Bi-Co-Ni-U and Cu-Bi vein mineralization at Wittichen, Schwarzwald, SW Germany: Geological setting, ore mineralogy, and fluid evolution. *Miner. Depos.* **47**, 251–276.
- Sverjensky D., Shock E. L. and Helgeson H. C. (1997) Prediction of the thermodynamic properties of aqueous metal complexes to 1000 C and 5 kb. *Geochim. Cosmochim. Acta* **61**, 1359–1412.
- Tagirov B. R., Zotov A. and Akinfiyev N. (1997) Experimental study of dissociation of HCl from 350 to 500° C and from 500 to 2500 bars: Thermodynamic properties of HCl°(aq). *Geochim. Cosmochim. Acta* **61**, 4267–4280.
- Thoenen T., Hummel W., Berner U. and Curti E. (2014) The PSI/Nagra Chemical Thermodynamic Database 12/07.
- Tian G. and Rao L. (2009) Spectrophotometric and calorimetric studies of U(VI) complexation with sulfate at (25 to 70) °C. *J. Chem. Thermodyn.* **41**, 569–574.
- Timofeev A., Migdisov A. A. and Williams-Jones A. E. (2015) An experimental study of the solubility and speciation of niobium in fluoride-bearing aqueous solutions at elevated temperature. *Geochim. Cosmochim. Acta* **158**, 103–111. Available at: <http://dx.doi.org/10.1016/j.gca.2015.02.015>.
- Timofeev A., Migdisov A. A., Williams-Jones A. E., Roback R., Nelson A. T. and Xu H. (2018) Uranium transport in acidic brines under reducing conditions. *Nat. Commun.* **9**, 2–8.
- Vercouter T., Vitorge P., Amekraz B. and Moulin C. (2008) Stoichiometries and thermodynamic stabilities for aqueous sulfate complexes of U(VI). *Inorg. Chem.* **47**, 2180–2189.
- Vopálka D., Štamberg K., Motl A. and Drtinová B. (2010) The study of the speciation of uranyl-sulphate complexes by UV-Vis absorption spectra decomposition. *J. Radioanal. Nucl. Chem.* **286**, 681–686.
- Xu H., Navrotsky A., Nyman M. and Nenoff T. (2000) Thermochemistry of microporous silicotitanate phases in the Na<sub>2</sub>O–Cs<sub>2</sub>O–SiO<sub>2</sub>–TiO<sub>2</sub>–H<sub>2</sub>O system. *J. Mater. Res.* **15**, 815–823.
- Zanonato P. L., Di Bernardo P., Bismondo A., Liu G., Chen X. and Rao L. (2004) Hydrolysis of

Uranium(VI) at Variable Temperatures (10-85 °C). *J. Am. Chem. Soc.* **126**, 5515–5522.

Zhang L., Liu C., Fayek M., Wu B., Lei K., Cun X. and Sun L. (2017) Hydrothermal mineralization in the sandstone–hosted Hangjinqi uranium deposit, North Ordos Basin, China. *Ore Geol. Rev.* **80**, 103–115.

Zhou W., Apted M. J. and Kessler J. H. (2010) The thermal-hydrological impact on increased spent-fuel storage capacity in Yucca mountain repository. *Nucl. Technol.* **170**, 336–352.